


# Early Eocene magnetostratigraphy and tectonic evolution of the Xining Basin, NE Tibet

Niels Meijer<sup>1</sup>  | Guillaume Dupont-Nivet<sup>2</sup> | Alexis Licht<sup>3</sup> | Pierrick Roperch<sup>2</sup> | Alexander Rohrmann<sup>4</sup> | Aijun Sun<sup>5,6,7</sup> | Shengcheng Lu<sup>8</sup> | Amber Woutersen<sup>9</sup> | Norbert Nowaczyk<sup>10</sup>

<sup>1</sup>Senckenberg Biodiversity and Climate Research Centre (SBIK-F), Frankfurt am Main, Germany

<sup>2</sup>Géosciences Rennes - UMR CNRS 6118, Univ Rennes, CNRS, Rennes, France

<sup>3</sup>CNRS, IRD, INRAE, CEREGE, Aix Marseille University, Aix-en-Provence, France

<sup>4</sup>Institute of Geological Sciences, Freie Universität Berlin, Berlin, Germany

<sup>5</sup>Key Laboratory of Western China's Environmental Systems (Ministry of Education), College of Earth and Environmental Sciences, Lanzhou University, Lanzhou, China

<sup>6</sup>Key Laboratory of Desert and Desertification, Northwest Institute of Eco-Environment and Resources, Chinese Academy of Sciences, Lanzhou, China

<sup>7</sup>University of Chinese Academy of Sciences, Beijing, China

<sup>8</sup>School of Urban Construction and Environment, Dongguan City College, Dongguan, China

<sup>9</sup>Department of Ecosystem and Landscape Dynamics (ELD), Institute for Biodiversity and Ecosystem Dynamics (IBED), University of Amsterdam, Amsterdam, the Netherlands

<sup>10</sup>GFZ German Research Centre for Geosciences, Potsdam, Germany

## Correspondence

Niels Meijer, Senckenberg Biodiversity and Climate Research Centre (SBIK-F), Senckenberganlage 25, D-60325 Frankfurt am Main, Germany.  
Email: [niels.meijer@senckenberg.de](mailto:niels.meijer@senckenberg.de)

## Funding information

European Research Council; Hessisches Ministerium für Wissenschaft und Kunst

## Abstract

The Cenozoic strata of the Xining Basin, NE Tibet, have provided crucial records for understanding the tectonic and palaeo-environmental evolution of the region. Yet, the age of the lower part of the sedimentary stratigraphy and, consequently, the early tectonic evolution of the basin remain debated. Here, we present the litho- and magnetostratigraphy of various early Eocene sections throughout the Xining Basin independently constrained by the U–Pb radiometric age of a carbonate bed. Our study extends the dated stratigraphy down to 53.0 Ma (C24n.1r) and reveals highly variable accumulation rates during the early Eocene ranging from 0.5 to 8 cm/ka. This is in stark contrast to the low but stable accumulation rates (2–3 cm/ka) observed throughout the overlying Palaeogene and Neogene strata. Such a pattern of basin infill is not characteristic of flexural subsidence as previously proposed, but rather supports an extensional origin of the Xining Basin with multiple depocentres, which subsequently coalesced into a more stable and slowly subsiding basin. Whether this extension was related to the far-field

This is an open access article under the terms of the [Creative Commons Attribution](https://creativecommons.org/licenses/by/4.0/) License, which permits use, distribution and reproduction in any medium, provided the original work is properly cited.

© 2022 The Authors. *Basin Research* published by International Association of Sedimentologists and European Association of Geoscientists and Engineers and John Wiley & Sons Ltd.

effects of the subducting Pacific Plate or the India–Asia collision remains to be confirmed by future studies.

#### KEYWORDS

Eocene, geochronology, northeast Tibet, palaeomagnetism, stratigraphy, Xining Basin

## 1 | INTRODUCTION

The Xining Basin, located on the north-eastern margin of the Tibetan Plateau, has provided valuable Cenozoic sedimentary records which have been extensively studied for reconstructing the evolution of atmospheric moisture (Abels et al., 2011; Bosboom et al., 2014; Dupont-Nivet et al., 2007; Fan et al., 2019; Fang et al., 2015; Meijer et al., 2019; Yang, Yang, et al., 2019), temperature (Page et al., 2019), vegetation (Dupont-Nivet, Hoorn, et al., 2008; Hoorn et al., 2012; Licht, Dupont-Nivet, et al., 2020), dust fluxes (Licht et al., 2014, 2016; Meijer et al., 2021; Ruan et al., 2019) and the tectonic history of the region (Dai et al., 2006; Dupont-Nivet et al., 2004; Dupont-Nivet, Dai, et al., 2008; Fan et al., 2019; He et al., 2021; Horton et al., 2004; Yang et al., 2017; Yang, Guo, et al., 2019; Zhang et al., 2016). However, age models for the early evolution of the basin remain unclear because the Xiejia section, which is the longest and most continuous section in the basin and therefore often cited for the age model (Dai et al., 2006; Meijer et al., 2019; Yang, Guo, et al., 2019), is underlain by a fault and lacks the lowermost stratigraphy.

This has important implications for understanding the tectonic origin of the basin which has been argued to be formed by flexure (e.g. He et al., 2021; Liu, Zhang, Pan, et al., 2013), extensional normal faults (Fan et al., 2019) or transtension (Wang et al., 2013, 2016; Zhang et al., 2016). In turn, these tectonic processes may be related to the far-field effects of either the Pacific Plate subduction or the India–Asia collision and are therefore crucial for understanding the active tectonic drivers in the region. Especially because well-dated early Eocene deposits are rare in the north-eastern Tibetan Plateau ever since the age model of the Qaidam Basin has been up for debate (e.g. Cheng et al., 2021) with one interpretation suggesting an early Eocene origin (e.g. Ji et al., 2017; Yin et al., 2008) and the other an Oligocene-to-Miocene time of formation (Nie et al., 2020; Wang et al., 2017). Therefore, improved age constraints and basin evolution reconstructions are needed to test the competing tectonic models in this region. Here, we present a basin-scale litho- and magnetostratigraphic study of the Xining Basin to reconstruct the early Eocene evolution of the basin. We

### Highlights

- The magnetostratigraphy of the Xining Basin is extended down to 53.0 Ma (C24n.1r).
- This early Eocene age is constrained by the U–Pb age of a lacustrine carbonate of  $53.7 \pm 3.3$  Ma.
- The lithostratigraphy and age model imply an extensional origin for the basin.

constrain our age model with a radiometric age derived from a carbonate bed.

## 2 | GEOLOGIC SETTING

The modern day Xining Basin is located on the north-eastern margin of the Tibetan Plateau and is bounded by the Riyue Shan in the west, the Daban Shan (eastern Qilian Shan) in the north and the Laji Shan in the south (Figure 1a). During the Mesozoic, the basin was part of the Xining-Minhe Basin which stretched towards Lanzhou in the east and to Guide in the south (Horton et al., 2004). Mesozoic strata include Middle Jurassic mudrocks and sandstones interlayered with coal beds, which are exposed only in the centre of the Xining Basin (Figure 1b; QBGMR, 1985). These are unconformably overlain by the Early Cretaceous Hekou Group and the Late Cretaceous Minhe Formation with another unconformity separating the two units (Figure 1c). Both consist of red mudrocks, sandstones and conglomerates and are observed to coarsen towards the south (Horton et al., 2004; QBGMR, 1985).

During the Cenozoic, the Xining Basin formed the western part of the Longzhong Basin which extended towards the Liupan Shan in the east and the Western Qinling Shan in the south (Horton et al., 2004). Palaeogene strata comprise the Xining Group and include red mudrocks, sandstones and gypsum beds of the Qijiachuan, Honggou, Mahalagou and Xiejia Formations (sensu Fang, Fang, et al., 2019; Figure 1c). The boundary between the Cretaceous and Palaeogene strata is reported as an angular unconformity in some locations and a disconformity in others (He et al., 2021; QBGMR, 1985).

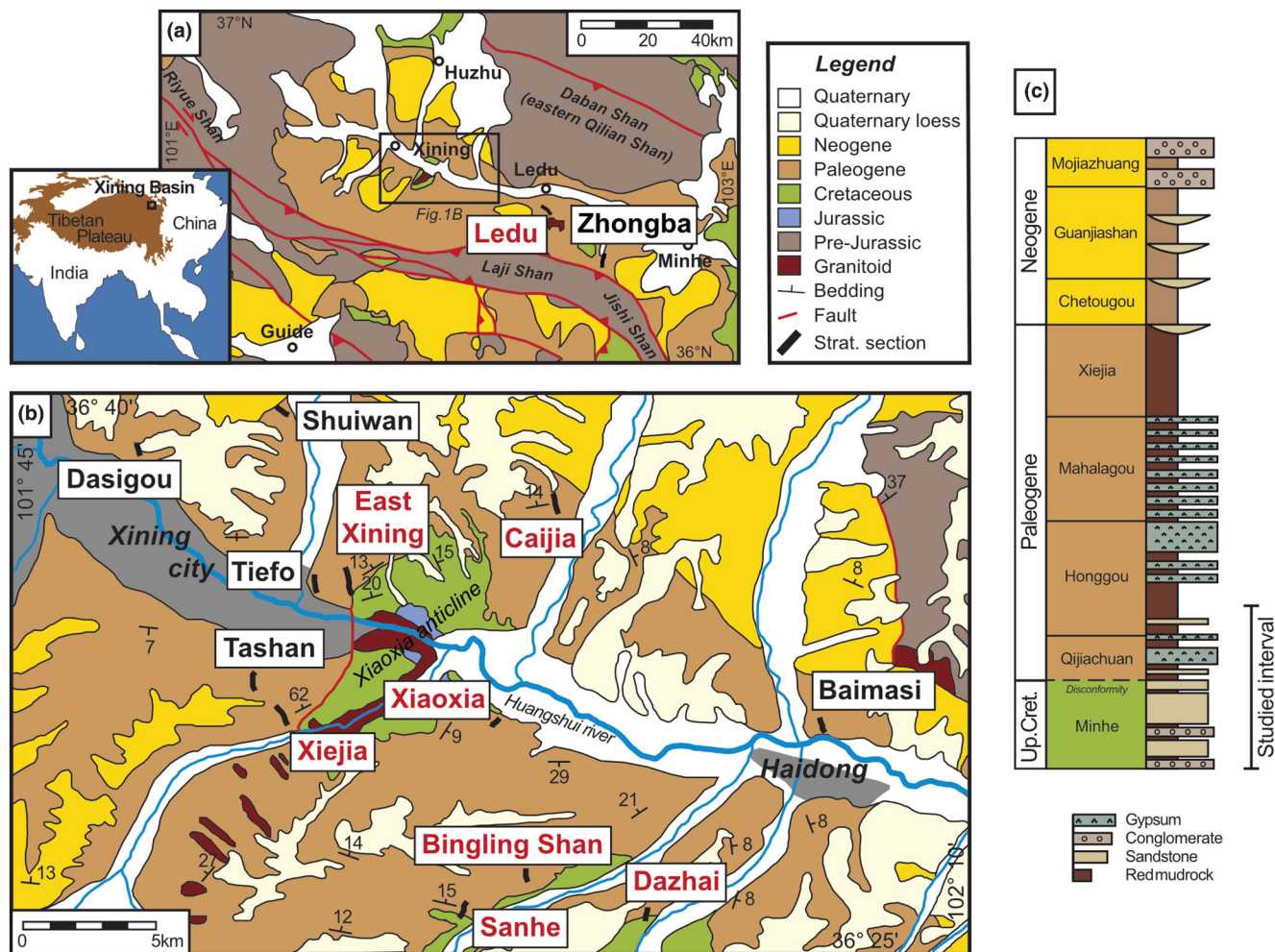


**FIGURE 1** (a) Geological map of the Xining Basin (modified from Fan et al., 2019) showing the location of the studied Ledu section. The inset map shows the location of the Xining Basin. (b) Detailed geological map (modified from BGMRQP, 1965; QBGMR, 1985) showing the section locations near Xining city. Sections used in this study are indicated in red. (c) Generalized lithostratigraphic column of the Xining Basin (based on Fang, Galy, et al., 2019; Horton et al., 2004; QBGMR, 1985).

Detrital zircons indicate that the Palaeogene sediments were derived from both the Qilian Shan in the north and the Western Qinling Shan in the south (He et al., 2021; Zhang et al., 2016). Subsequent Neogene deformation resulted in the uplift of the Laji Shan, which segmented the Longzhong Basin into smaller sub-basins (Horton et al., 2004; Lease et al., 2011). Neogene transpression in the Xining Basin resulted in several basement-cored folds such as the Xiaoxia anticline which exposes the stratigraphy (Figure 1b; Zhang & Cunningham, 2013). Neogene strata comprise the Guide Group and include mudrocks, sandstones and conglomerates of the Chetougou, Guanjiashan and Mojiazhuang Formations (sensu Fang, Fang, et al., 2019; Figure 1c). Locally, an additional Neogene conglomeratic succession, termed the Zhongba Formation, has been recognized in the foothills of the south-eastern Xining Basin unconformably overlying the Palaeogene strata (He et al., 2021).

### 3 | METHODS

#### 3.1 | Sections and sampling

We have studied the litho- and magnetostratigraphy of the Ledu section located in the eastern part of the Xining Basin (Figure 1a) and the following sections in the western part near Xining city (Figure 1b): Xiaoxia, Bingling Shan (lithostratigraphy previously studied by Dai et al., 2006), Sanhe (lithostratigraphy previously studied by Zhang et al., 2016) and Dazhai (lithostratigraphy previously studied by Horton et al., 2004, and Zhang et al., 2016). We correlate these with the previously studied Xiejia, East Xining and Caijia sections (Meijer et al., 2019). Detailed GPS coordinates can be found in the Supporting Information. The lithostratigraphy was described in the field and palaeomagnetic samples were collected at ca. 0.5 to 2 m resolution using an electric

hand drill. The orientations of the palaeomagnetic samples were measured using a compass mounted on an orientation stage. In addition, hand-sized rock samples were collected for rock magnetic analyses at Ledu and the previously studied Caijia section (Meijer et al., 2019) with a resolution of ca. 2 to 5 m.

### 3.2 | U–Pb dating of lacustrine carbonates

Fifteen lacustrine carbonates were collected throughout the sections for radiometric dating. The samples were cut to expose fresh surfaces and then incorporated into a 1-inch epoxy mount for in situ U–Pb dating. The mounts were then manually polished, first with coarse then fine (5  $\mu\text{m}$  grit size) sandpaper. U–Pb dating was conducted by laser ablation inductively coupled plasma mass spectrometry (LA-ICP MS) at the TraceLab laboratory of the University of Washington. Hardware description, acquisition procedure, reference materials and data reduction steps are described in Cong et al. (2021). Uncertainties are analytical and do not include the systematic uncertainty calculated from the long-term reproducibility of secondary reference materials due to the current lack of international carbonate reference materials. The systematic uncertainty based on the long-term reproducibility of 10 zircon reference materials is ca. 2.67% ( $2\sigma$ ) for  $^{238}\text{U}/^{206}\text{Pb}$  ratios at the University of Washington (Licht, Win, et al., 2020).

### 3.3 | Rock magnetism

The palaeomagnetic samples of the Bingling Shan and Sanhe sections were analysed at the Archeo-Paleomagnetic laboratory of Géosciences Rennes, France, the Dazhai section at the Paleomagnetic Laboratory 'Fort Hoofddijk' of the Faculty of Geosciences at Utrecht University, the Netherlands, and the Ledu section at the Laboratory of Rock- and Paleomagnetism at the German Research Center for Geosciences (GFZ) in Potsdam. After measuring magnetic susceptibility, the samples were thermally demagnetized by stepwise heating up to 650°C using a MMTD48 in Rennes and an ASC Scientific TD48 in Utrecht and Potsdam. The natural remanent magnetization (NRM) was measured after every step using a superconducting quantum interference device (SQUID). The magnetic susceptibilities of the samples were measured before the thermal demagnetization using a Bartington MS2 for the samples measured at Géosciences Rennes, and an AGICO Multifunction Kappabridge MFK-1A for the samples measured at the GFZ.

The hand samples of the Ledu and Caijia sections were carefully ground using a mortar and pestle and packed in cubic plastic boxes of 6  $\text{cm}^3$ . Isothermal remanent magnetizations (IRM) were imparted using a 2G Enterprises 660 pulse magnetizer and subsequently measured using a Molspin spinner magnetometer. The IRM intensity acquired at 1.5 T is defined here as the saturation IRM (SIRM) and, together with the IRM intensity acquired at a reversed field of 0.2 T, is used to define the S-ratio as:  $0.5 \times (1 - [\text{IRM}_{-0.2\text{T}}/\text{SIRM}_{1.5\text{T}}])$ . Detailed IRM acquisition curves were measured for selected samples using a 4" Princeton Measurements Corporation 'Micromag' alternating gradient magnetometer (AGM). These S-ratios and IRM acquisition are used to characterize the magnetic components throughout the record.

## 4 | RESULTS

### 4.1 | Lithostratigraphy and depositional environment

The lithostratigraphy of all sections is subdivided into formations and members following QBGMR (1985) and presented in Figure 2. The East Xining, Xiejia and Caijia sections are from Meijer et al. (2019). The lithofacies are described and the depositional environment is interpreted below.

#### 4.1.1 | Upper Minhe Formation ( $\text{K}_2\text{m}^3$ )

##### *Description*

The upper Minhe Formation consists of dm- to m-scale beds of sandstone and conglomerate (Figure 3a–d). Some m-scale channels are observed in the sandstones. The conglomerates are both clast and matrix supported and are composed of poorly sorted, subangular-to-subrounded polyimictic pebbles (Figure 3d). The sandstones are medium- to coarse-grained and poorly sorted containing subrounded granules and pebbles. The sedimentary structure is predominantly massive, but trough cross-bedding and horizontal bedding are observed occasionally as well (Figure 3c). The sandstones and conglomerates are interbedded with rare dm-scale beds of massive red mudrocks. These mudrocks become more abundant towards the north (Figure 3e).

##### *Interpretation*

The matrix-supported conglomerates in the upper Minhe Formation are interpreted as debris flow deposits and the clast-supported conglomerates and sandstones as braided river channel fills (Smoot & Lowenstein, 1991).



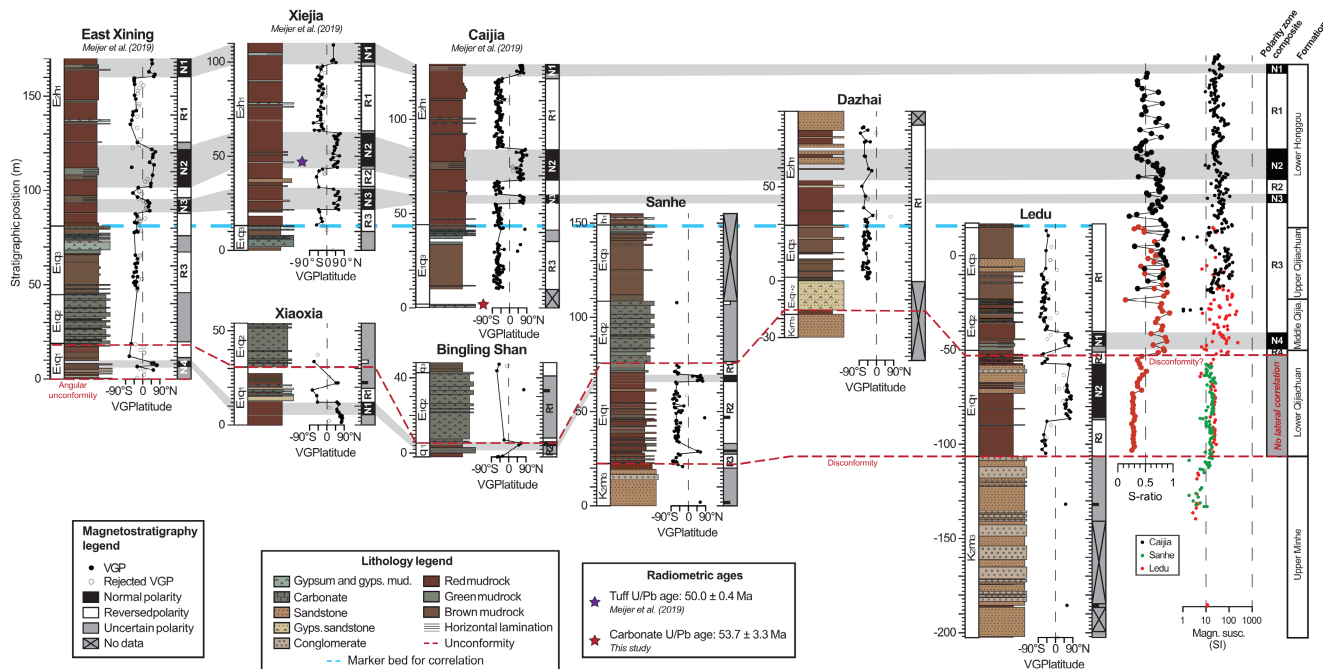


**FIGURE 2** Litho- and magnetostratigraphy of the studied sections. The East Xining, Xieja and Caijia sections are from Meijer et al. (2019). The blue dashed line indicates the transition between the Qijiachuan and Honggou Formations which is used as a marker bed for correlating the sections. Rock magnetic properties are shown on the right as well as a composite of the polarity zones which are correlated with the geomagnetic polarity timescale in Figure 8.

Consequently, the depositional environment of the upper Minhe Formation is interpreted as a proximal alluvial fan. The sediments are likely transported from the south as the upper Minhe Formation is fining towards the north (QBGMR, 1985).

#### 4.1.2 | Lower Qijiachuan Formation ( $E_1q^1$ )

##### Description

The Minhe Formation is overlain by the Qijiachuan Formation. At most locations, this boundary is represented by a disconformity (Figure 3a,b), which may span ca. 20 Ma according to the magnetostratigraphy in the eastern Xinin Basin (He et al., 2021). An angular unconformity is observed in the East Xining section (Figure 3e). The lithofacies of the lower Qijiachuan Formation consist predominantly of massive red mudrocks containing slickensides due to swelling clays. In the western sections, these mudrocks occasionally contain cm- to dm-scale horizons of mottling (Figure 3f) in red (2.5YR 4/4), purplish (7.5R 4/3), yellow (2.5Y 5/4), grey (10GY 5/1) and dark grey (10B 3/1). The mudrocks are commonly interbedded with laterally extensive dm- to m-scale sandstone beds. These sandstones are medium-to-coarse grained, contain granules and have a massive, horizontal bedded or trough cross-bedded structure. Occasionally, the mudrocks and sandstones

are interbedded with cm-scale carbonate beds containing a horizontally laminated or massive structure.

##### Interpretation

The fine-grained deposits in the lower Qijiachuan Formation indicate low-energy suspension settling and we interpret the depositional environment as a distal alluvial mudflat (Abels et al., 2011; Dupont-Nivet et al., 2007; Smoot & Lowenstein, 1991; Talbot et al., 1994). The mottled horizons and slickensides suggest that some of the mudrocks have been subjected to pedogenesis. The sandstones are interpreted as unconfined fluvial flows based on their lateral extent (North & Davidson, 2012). The carbonates may have formed in a lacustrine setting resulting in horizontal laminations or due to spring water as they are often observed to overlie the more porous sandstone beds (Smoot & Lowenstein, 1991).

#### 4.1.3 | Middle Qijiachuan Formation ( $E_1q^2$ )

##### Description

The middle Qijiachuan Formation is characterized by a ca. 30-m-thick package of organic-rich gypsum beds in the western part of the Xining Basin (Figure 3a,g) and previously described in Meijer et al. (2019). These beds have a massive-to-nodular structure and alternate on a dm scale between light grey and darker grey beds due



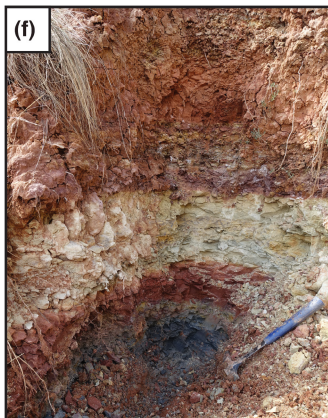
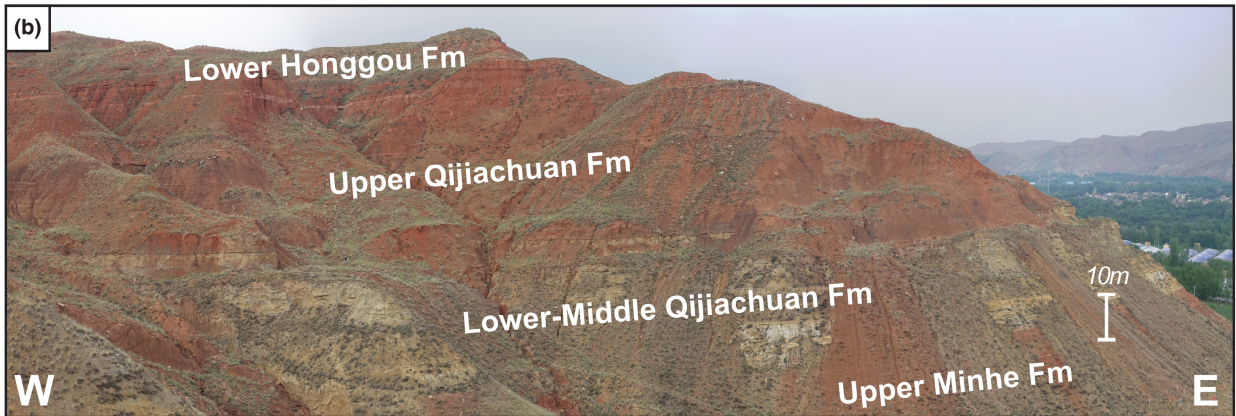
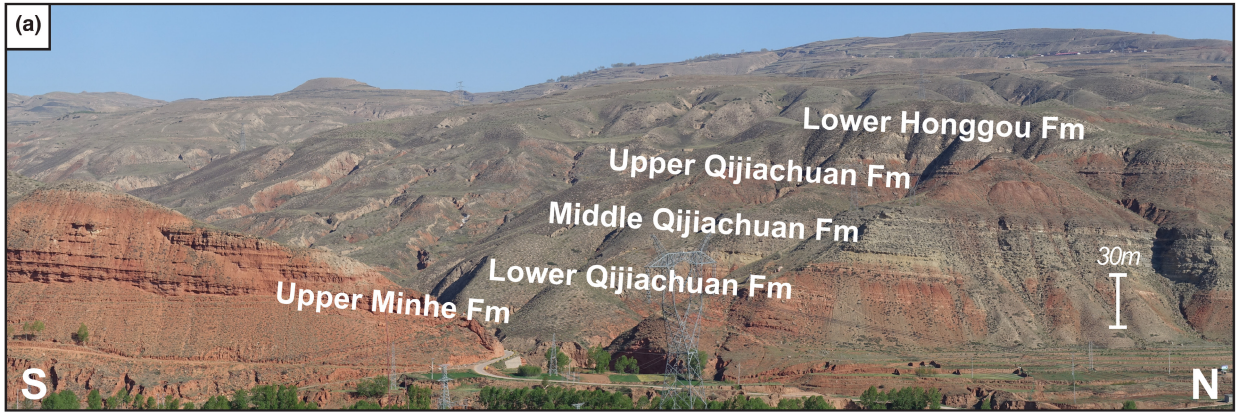




**FIGURE 3** Pictures of the studied sections and lithofacies. (a) Overview of the Sanhe section. (b) Overview of the Dazhai section. (c) Sandstone of the Minhe Formation at –150 m level of the Ledu section. Jacob's staff with 10-cm-spaced markings for scale. (d). A conglomerate of the Minhe Formation at the Ledu section showing the polymictic composition of the clasts. Pencil for scale. (e) Overview of the base of the East Xining section showing an angular unconformity between the Minhe and Qijiachuan Formations. (f) Yellow-white siltstone and variegated mudrocks at the 47 m level of the Sanhe section. Hammer for scale. (g) The middle Qijiachuan Formation at Bingling Shan showing alternations between light grey and darker grey gypsiferous mudrocks and gypsum beds. Secondary gypsum forms the white powdery coatings and fracture-filling fibrous gypsum forms the horizontal veins. Hammer for scale. (h) Top of the Qijiachuan Formation at the Xiejia section showing liver-brown and green mudrocks interbedded with cm-scale carbonate beds and the transition to the brick-red mudrocks of the Honggou Formation. Person for scale.

to varying content in gypsum and organic materials (ca. 0.1%–1.7%). The top ca. 2 m of this package consists of horizontally laminated gypsum interbedded with cm-scale carbonates. Towards the east, the lithofacies of the middle Qijiachuan Formation vary considerably. In the Dazhai section, the lithofacies consists of ca. 15 m of gypsiferous, medium-grained sandstone with a massive structure (Figure 3b). This is overlain by ca. 3 m of organic-rich gypsiferous mudrocks. The gypsiferous sandstone is a local feature and the organic-rich gypsum package reappears but is observed to thin towards the east. At the Ledu section, located ca. 30 km further towards the east, these characteristic gypsum beds are lacking completely. Instead, the lithofacies consist of red and grey massive mudrocks alternated with meter-scale intervals of dark grey, horizontally laminated mudrocks with a relatively high organic content (0.4%) and interbedded with cm-scale beds of nodular gypsum and carbonate.

#### Interpretation

Based on the abundance of evaporites, we interpret the depositional environment of the middle Qijiachuan in the western part of the Xining Basin as a saline lake with the varying TOC reflecting fluctuations in salinity and/or productivity (Meijer et al., 2019). The abundance of sandstones at the Dazhai section indicates local fluvial deposition. The massive mudrocks at the Ledu section are interpreted as a distal alluvial mudflat alternated with intervals of lacustrine deposition as indicated by the horizontally laminated mudrocks (Abels et al., 2011; Dupont-Nivet et al., 2007; Meijer et al., 2019; Smoot & Lowenstein, 1991).

#### 4.1.4 | Upper Qijiachuan Formation ( $E_1q^3$ )

##### Description

The boundary to the upper Qijiachuan Formation can be identified by a shift to mudrocks with a characteristic dark reddish-brown colour (Figure 3a,b,h), termed liver brown in QBGMR (1985) and occurring throughout the basin. The mudrocks are massive and contain slickensides, rare carbonate nodules and are interbedded with

cm-scale cross-laminated siltstones and dm-scale cross-bedded sandstones. The mudrocks have a relatively high organic content varying between 0.2% and 0.6%. In the western part of the basin, the top of the upper Qijiachuan Formation is characterized by dm-scale massive gypsum beds and green mudrocks alternated with cm-scale carbonate beds (Figure 3h).

##### Interpretation

The depositional environment is interpreted as an organic-rich distal alluvial mudflat (Meijer et al., 2019). The organic material results in the liver-brown colour of the mudrocks. The slickensides and carbonate nodules indicate subaerial exposure and pedogenesis. The silt- and sandstones indicate episodic fluvial activity by unconfined flows (North & Davidson, 2012). The top of the formation is interpreted as lacustrine deposits in saline-to-alkaline environment (Meijer et al., 2019).

#### 4.1.5 | Lower Honggou Formation ( $E_2h^1$ )

##### Description

The transition to the lower Honggou Formation is marked by a shift to brick-red coloured mudrocks with a massive structure (Figure 3a,b,h). This distinct shift can be recognized throughout the basin and is used as a marker bed to correlate the sections (blue dashed line in Figure 2). The Honggou Formation has been described previously in Meijer et al. (2019) and will be summarized here. The red mudrocks are interbedded with m-scale intervals of brown-coloured, horizontally laminated mudrocks, cm-scale carbonate beds and occasional dm-scale sandstone and gypsum beds. At the Dazhai section, we observe abundant dm- to m-scale sandstone beds, which are laterally extensive, medium- to coarse-grained, and have a massive or trough cross-bedded structure.

##### Interpretation

The depositional environment of the red mudrocks is interpreted as an alluvial mudflat alternated with alkaline to saline lacustrine conditions and occasional fluvial deposits (Meijer et al., 2019). The Dazhai section is interpreted

as a more proximal setting as evidenced by the more abundant fluvial sandstones.

## 4.2 | Radiometric dating and magnetostratigraphy

### 4.2.1 | U–Pb radiometric age

Meijer et al. (2019) radiometrically dated a tuff layer in the Honggou Formation at the Xiejia section, which constrained the age to  $50.0 \pm 0.4$  Ma (Figure 2). Here, we provide an additional radiometric age of a carbonate bed, CJC07, located at the top of the middle Qijiachuan Formation in the Caijia section (1.3 m level; Figure 2). This was the only sample out of the 15 that were measured that contained enough uranium. The age was determined from the lower intercept on the Tera–Wasserburg plot (Figure 4). The resulting age is  $53.7 \pm 3.3$  Ma ( $2\sigma$ ; MSWD: 0.4).

### 4.2.2 | Rock magnetism

The mudrocks sampled for magnetostratigraphy show an abrupt shift in rock magnetic properties occurring at the transition between the lower and middle Qijiachuan Formation. This shift is obscured in the western sections

due to the low-magnetic signal of evaporites in the middle Qijiachuan Formation, but can be clearly identified in the mudrocks of the Ledu section. Magnetic susceptibilities increase abruptly from ca.  $20 \times 10^{-5}$  to ca.  $200 \times 10^{-5}$  SI, while S-ratios increase to mostly  $>0.5$  (Figure 2) and NRM increases to  $>10^{-3}$  A/m (Figure S1). Magnetic susceptibilities remain relatively high throughout in the upper Qijiachuan Formation and gradually decrease down to ca.  $20 \times 10^{-5}$  SI in the Honggou Formation.

Thermal demagnetization resulted in the removal of a viscous normal overprint up to ca.  $200^\circ\text{C}$  (Figure 5). High-susceptibility samples show a drop in NRM at ca.  $580^\circ\text{C}$ , indicating that magnetite is the main magnetic carrier. Samples with both high- and low-magnetic susceptibilities require temperatures beyond  $650^\circ\text{C}$  to completely demagnetize, which indicates the ubiquitous presence of haematite throughout the record. The abrupt transition observed in the S-ratios and magnetic susceptibilities of the Qijiachuan Formation thus represents a shift from haematite to magnetite as the dominant magnetic carrier. This is further supported by the IRM and hysteresis plots which show wasp-waisted loops due to a combination of different coercivities (e.g. Roberts et al., 1995) which can be unmixed in a soft component of magnetite and a hard component representing haematite (Figures 6, S2 and S3). In samples with a significant fraction of magnetite, the hysteresis parameters Bcr/Bc and Mrs/Ms are in the range 1.9–2.2 and 0.24–0.3, respectively,

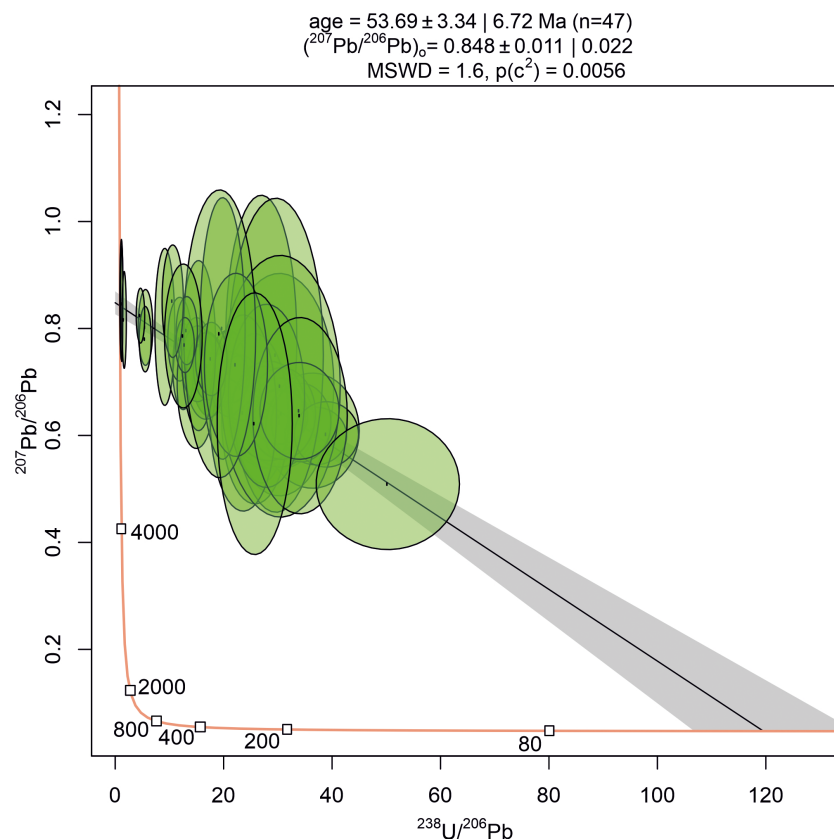
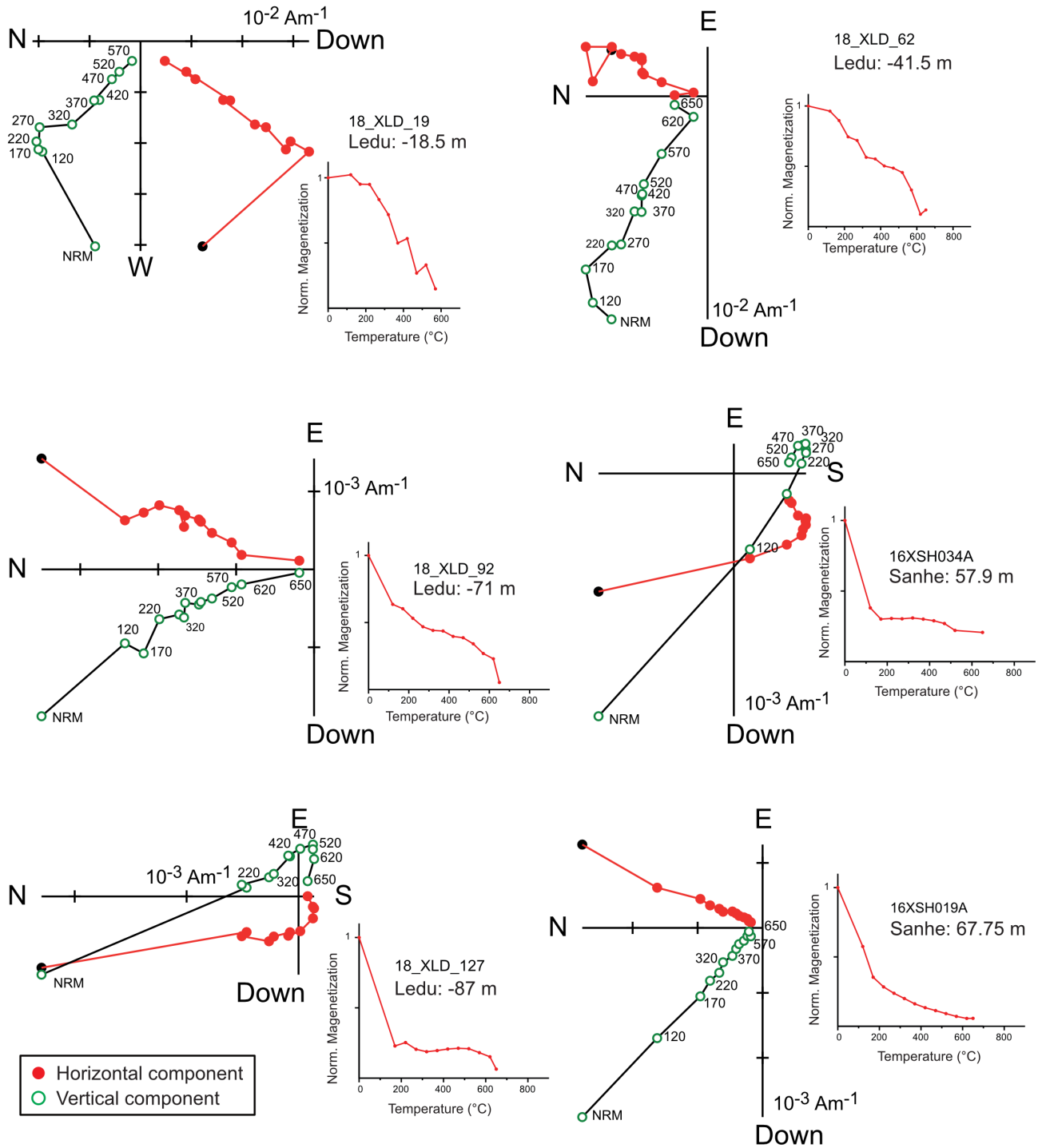


FIGURE 4 Tera–Wasserburg diagram of the lacustrine carbonate sample CJC07.





**FIGURE 5** Orthogonal plots of thermal demagnetization for six representative samples of the Ledu and Sanhe sections. Numbers indicate temperature steps in °C. Samples 18XLD19 and 18XLD62 from the Ledu section have magnetite as the main magnetic carrier, while the other samples are dominated by haematite. The coordinates of the plots are in situ.

suggesting fine-grained single- to pseudo-single-domain magnetite. The low  $B_c$  value in haematite samples suggests that the haematite is very fine grained. Sandstones, conglomerates and gypsum beds do not preserve a stable remanent magnetization. This hampers reconstructing the magnetostratigraphy of the middle Qijiachuan Formation in the western part of the Xining Basin and the Minhe Formation.

#### 4.2.3 | ChRM directions

Characteristic remanent magnetization (ChRM) directions were calculated for each sample using eigenvector principal component analysis on at least four temperature steps showing a linear decay between ca. 300 and 650°C (Figure 5; Kirschvink, 1980). Similar polarities and

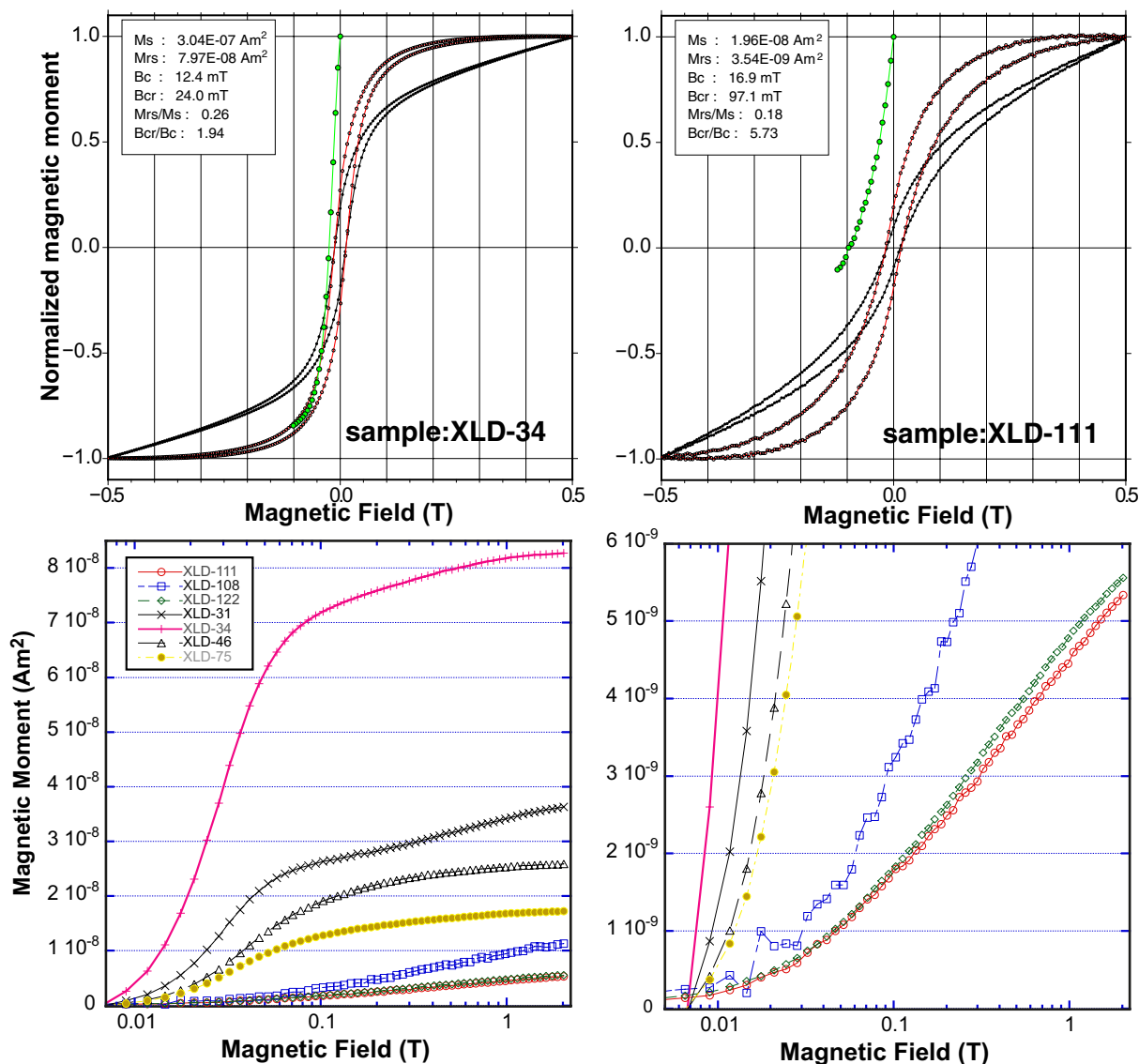


**FIGURE 6** High-field magnetic properties. (Top) Examples of hysteresis plots (black lines) for two samples of the Ledu section with magnetite (left) and haematite (right) as the dominant magnetic carrier, both showing a wasp-waisted loop. Red lines show the paramagnetic correction and green lines show the remanent curve. (Bottom) IRM acquisition for seven samples of the Ledu section. The plot on the right is a zoom to highlight the low amount of magnetization acquired below 0.1 T in samples at the base of the Ledu section (XLD-108, XLD-111 and XLD-122).

directions were observed in both the lower-temperature magnetite and the higher-temperature haematite components of each sample as also reported by Dai et al. (2006). The ChRMs were anchored to the origin and the directions resulting in a maximum angular deviation (MAD) of  $>30^\circ$  were rejected. However, most samples have a MAD of  $<10^\circ$ .

The ChRMs show two clusters with either normal or reversed directions (Figure 7). Mean directions were calculated using Fisher statistics (Fisher, 1953) and directions with an angle of more than  $45^\circ$  from the mean were rejected from further analysis (open symbols in Figure 2 and red symbols in Figure 7). We performed a reversals test (McFadden & McElhinny, 1990) on the

mean directions of the sections to check the reliability of our dataset. The test succeeded for the Sanhe section with classification C, but is indeterminate for the Xiaoxia section and failed for the Ledu and Bingling Shan sections. The poor performance of the reversals tests is due to an unresolved normal overprint which has been observed in previous magnetostratigraphic studies in the Xining Basin (Dupont-Nivet, Dai, et al., 2008; Meijer et al., 2019). This would exclude our dataset for the analysis of tectonic rotations but does not affect the reliability of the reversals used in our magnetostratigraphy. Only in the Xiaoxia section, we observe a cluster of normal directions similar to the modern day field, suggesting that these may have been completely remagnetized

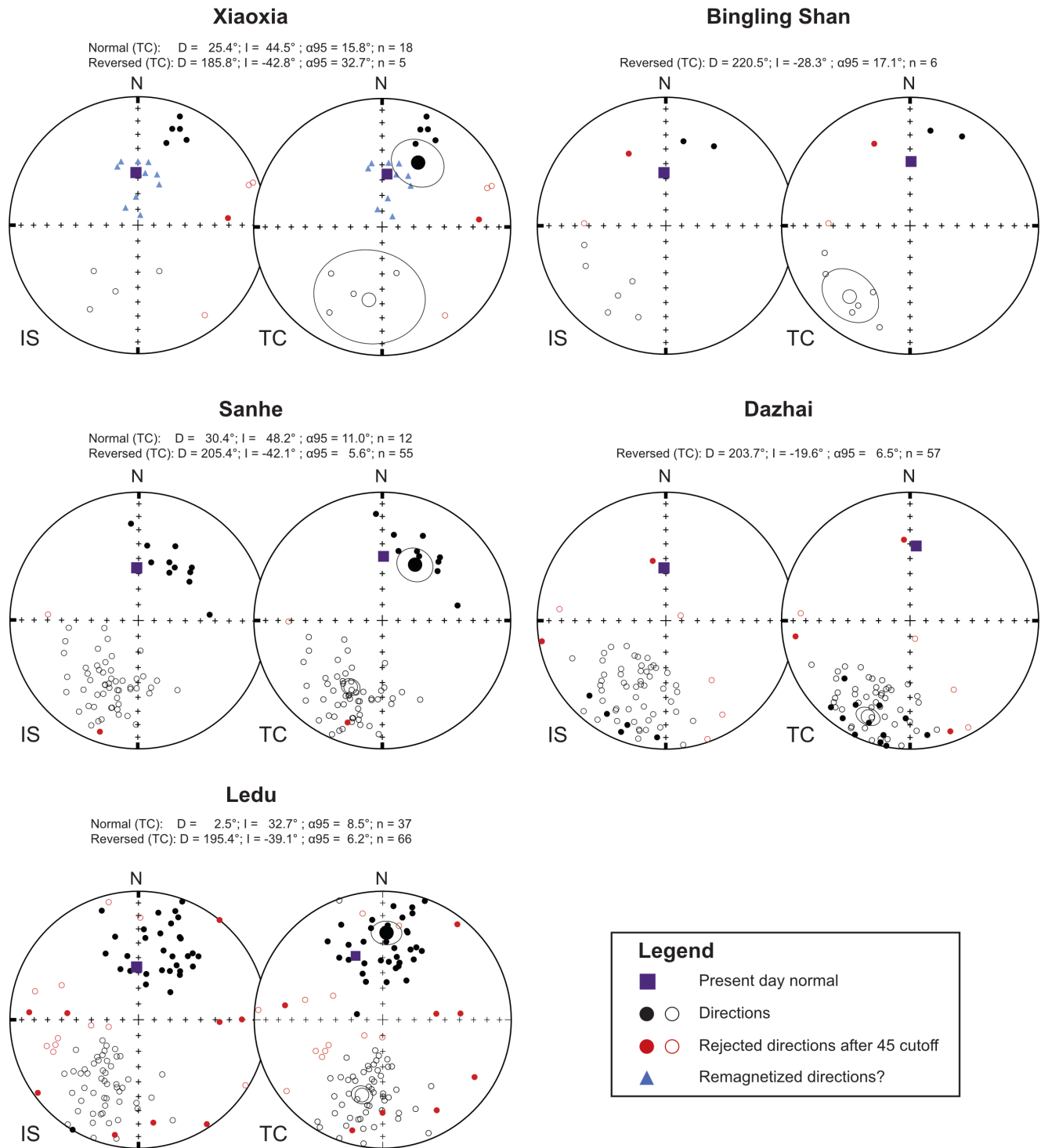


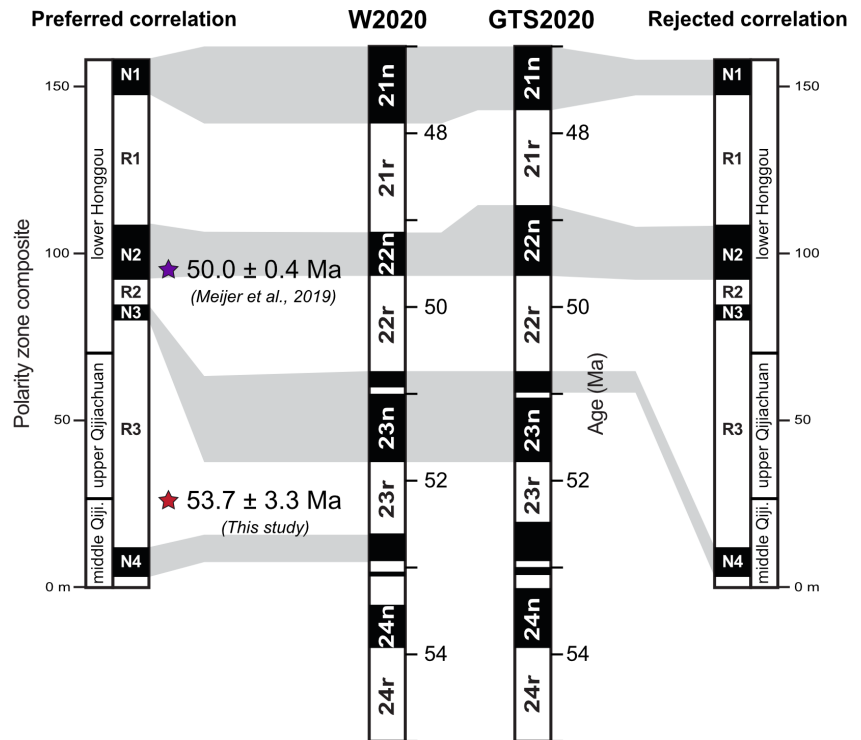
**FIGURE 7** Equal-area stereographic projections of calculated ChRM directions of the studied sections both in situ (IS) and tilt corrected (TC).

(blue symbols in Figure 7). These samples are from a weathered interval at the base of the section and are not considered a polarity zone in the magnetostratigraphy (Figure 2). Virtual geomagnetic poles (VGPs) were calculated from the ChRMs and are shown in Figure 2. Polarity zones are defined by at least two samples of the same polarity.

#### 4.2.4 | Correlations to the geomagnetic polarity timescale

In the following, we first correlate the polarity zones between the different sections to create a composite (Figure 2) and then correlate this to the geomagnetic polarity timescale (Figure 8). We use the two astronomically

**FIGURE 8** Magnetostratigraphic correlations to the astronomically tuned geomagnetic polarity timescales of W2021 (Westerhold et al., 2020) and GTS2020 (Speijer et al., 2020). Polarity zones represent a composite of the sections shown in Figure 2. Note that the overlying magnetostratigraphy of the Xining Basin extends up to the Neogene.



tuned timescales that are currently available, the GTS20 (Speijer et al., 2020) and W2020 (Westerhold et al., 2020), but note that there are only minor differences of <300 ka between the two (Figure 8).

The lower Honggou Formation contains three normal polarity zones (N1–N3 in the composite) which correlate well among the East Xining, Xiejia and Caijia sections (Meijer et al., 2019). Below is a long reversed polarity zone of up to 80 m (R3 in the composite). This zone correlates well with the Qijiachuan liver-coloured mudrocks of the East Xining, Caijia, Dazhai and Ledu sections. However, this zone is especially thick in the Dazhai section (R1) where it extends far into the overlying Honggou Formation. This interval contains abundant fluvial sandstones, which may indicate locally higher accumulation rates and therefore a thicker reversed zone compared to the other sections. The lower part of composite R3 is only recorded in the Ledu section (R1), where it is underlain by an 8-m-thick normal zone at the base of the middle Qijiachuan Formation (N1 in the Ledu section and N4 in the composite). The polarity zones in the lower Qijiachuan Formation are laterally inconsistent. At Ledu, this interval is characterized by a long normal zone bounded by reversed zones. But at Sanhe, this interval is mostly reversed with only two short normal polarity zones. The upper of these correlate with the East Xining, Xiaoxia and Bingling Shan sections, but not with the Ledu section. This may indicate more lateral variations in accumulation rates or gaps in the stratigraphic record because we note that the discrepancies between the polarity zones occur below the

shift in rock magnetic properties. This shift may therefore mark an unconformity and will be discussed in more detail below.

The magnetostratigraphy above can be extended up into the Neogene (Abels et al., 2011; Bosboom et al., 2014; Dai et al., 2006; Dupont-Nivet et al., 2007; Meijer et al., 2019; Xiao et al., 2012; Yang et al., 2017; Yang, Yang, et al., 2019). Following these studies, N1 and N2 have been correlated with C21n and C22n, respectively, which is further constrained by the radiometric age of a tuff layer in the Xiejia section (Figure 8; Meijer et al., 2019). N3 can then be correlated with C23n (following Yang, Yang, et al., 2019) and N4 with C24n.1n (preferred correlation in Figure 8). This correlation would put the dated carbonate at 52.5 Ma and therefore well within the radiometric age constraints of  $53.7 \pm 3.3$  Ma. However, polarity zone N3 does not fit the expected pattern of C23n, and this correlation results in highly variable accumulation rates ranging from 0.5 cm/ka in C23n to 7 cm/ka in C23r (Figure 9). Hence, alternatively, N3 was interpreted as remagnetized and R2 and R3 have been correlated with C22r by Meijer et al. (2019), while N4 could be correlated with C23n.1n (rejected correlation in Figure 8). This correlation would put the dated carbonate at 50.6 Ma and therefore also within the radiometric age constraints. However, it requires N3 to be ignored even though there is no evidence for remagnetization in both the lithologies and rock magnetic properties (Meijer et al., 2019). The intensity of the magnetization, unblocking temperatures and even the previously reported transformation of the magnetic minerals during heating at 500°C (Bosboom et al., 2014) are



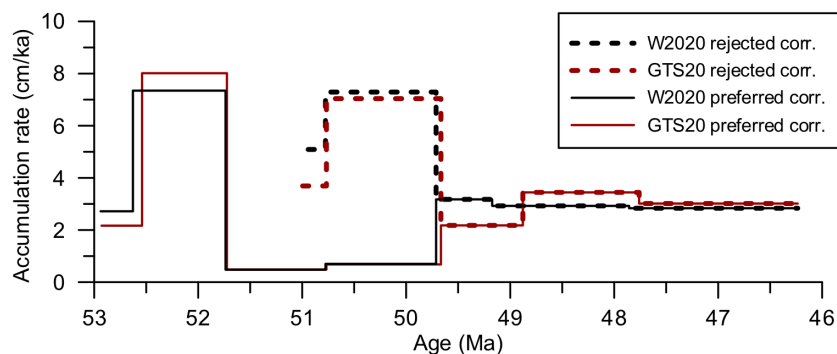


**FIGURE 9** Accumulation rates using the magnetostratigraphic correlations presented in this study and two astronomically tuned age models for the chron boundary ages (Speijer et al., 2020; Westerhold et al., 2020). Thicknesses of the polarity zones are derived from adding together the Ledu to the Caijia section at the Qijiachuan–Honggou transition (blue line in Figure 2).

observed in both normal and reverse polarities (Figure S4). Therefore, we do not observe remagnetization in these deposits except for the viscous overprint in the present-day field. Both correlations imply that accumulation rates are variable (Figure 9), but we consider our preferred correlation to be the most parsimonious because it implies no additional normal chrons.

Our preferred correlation results in an age of 53.0 Ma (C24n.1r) at the base of the middle Qijiachuan Formation. We note that the underlying magnetostratigraphic pattern at the Ledu section (N2) fits well with the expected pattern of C24n.3n, while the short normal zones at Sanhe (N1 and N2) fit with the expected pattern of C25n and C26n. However, due to the lateral inconsistency between the polarity zones at the Sanhe and Ledu sections and the lack of additional age constraints, we refrain from further interpreting these polarity zones.

## 5 | DISCUSSION

### 5.1 | Age model and basin infill

Our study extends the age model of the Xining Basin strata down to the early Eocene at 53.0 Ma. This age is older than the 49.3 Ma recorded at the Zhongba section in the eastern Xining Basin (He et al., 2021), but a more detailed comparison with this section is hampered by a lack of lithostratigraphic correlations. We also refine the age models of Dai et al. (2006) and Yang, Yang, et al. (2019), who interpreted the top of the Qijiachuan Formation as 53 Ma due to a viscous normal overprint recorded in the gypsiferous mudrocks at the base of the Xiejia section. In our magnetostratigraphy, the entire upper Qijiachuan Formation is reversed and the base of the Xiejia section corresponds to 52.0 Ma instead.

We observe an abrupt shift from a haematite- to magnetite-dominated magnetic assemblage at the base

of the middle Qijiachuan Formation. In the following, we discuss possible mechanisms for the appearance of this magnetite. As described above, we observe no evidence for remagnetization in these strata, except for the viscous normal overprint. This suggests that both magnetite and haematite have a detrital or early chemical origin soon after deposition. The transition to magnetite as the main magnetic carrier could thus represent a shift in provenance increasing the supply of detrital magnetite. A similar shift has been recognized in the Miocene strata of the Xining Basin where an increase in detrital magnetite was derived from plutonic and volcanic rocks from the uplifting Laji Shan and was coupled to unstable sedimentation rates and an unconformity (Xiao et al., 2012). Another increase in single-domain magnetite was observed at 51.7 Ma in the neighbouring Linxia Basin coeval with a shift in detrital zircons and linked to the uplift of the Western Qinling Shan (Figure 10; Feng et al., 2021, 2022). A similar change in provenance may explain the appearance of magnetite in the Xining Basin. However, the single- to pseudo-single-domain magnetic properties that we observe indicate that the magnetite in the Xining Basin is very fine grained and unlikely to withstand long-term sedimentary transport.

Alternatively, increased precipitation could have resulted in the formation and preservation of pedogenic magnetite as widely observed in the palaeosols of the Chinese Loess Plateau (e.g. Ahmed & Maher, 2018; Deng et al., 2004; Maher & Taylor, 1988). This could also explain the higher organic content corresponding to the higher-magnetic susceptibilities in the middle and upper Qijiachuan Formation and the gradual decrease in susceptibility in the overlying Honggou Formation which has been previously linked to drying (Fang et al., 2015). A pedogenic origin for some of the particles in this interval is supported by frequency-dependent susceptibility data, indicating the occurrence of ultrafine magnetic particles at the superparamagnetic to single-domain transition (Fang et al., 2015). However, we note that the shift to

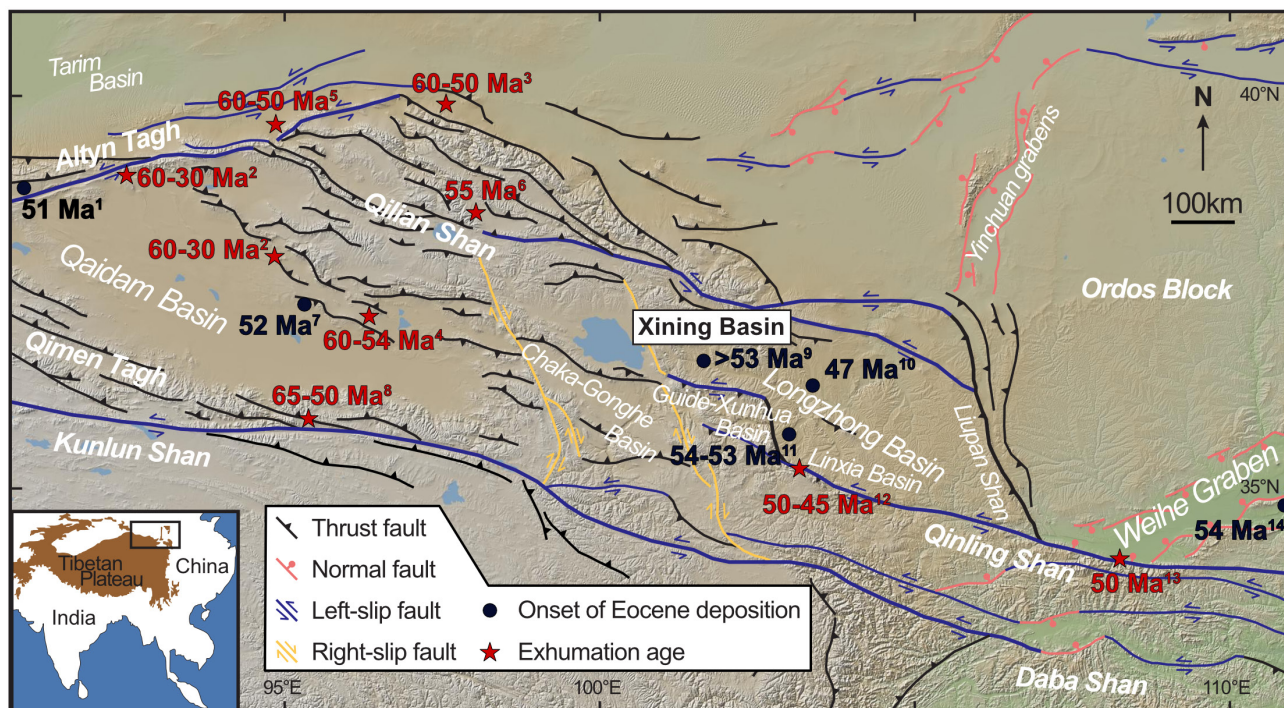


**FIGURE 10** Map of the north-eastern Tibetan Plateau showing tectonic events during the early Eocene: (1) Li et al. (2018); (2) Jolivet et al. (2001); (3) He et al. (2017); (4) He et al. (2018); (5) He et al. (2020); (6) Li et al. (2020); (7) Ji et al. (2017); (8) Staisch et al. (2020); (9) He et al. (2021) and this study; (10) Wang et al. (2016); (11) Feng et al. (2021); (12) Clark et al. (2010); (13) Liu, Zhang, Pan, et al. (2013); and (14) Chen et al. (2021). Modern day topographic base map is from the GeoMapApp software (Ryan et al., 2009) available at <http://www.geomapp.org/>. The faults are redrawn from Zuza and Yin (2016) and references therein.

higher-magnetic susceptibility also corresponds to higher NRM (Figure S1), which indicates a significant contribution of single-domain grains as well. The higher accumulation rates observed in this interval (Figure 9) may have played a role in reducing the time of subaerial exposure for the sediments. This could have improved the preservation of magnetite by both reducing the dissolution and oxidation of the magnetite minerals (e.g. Fang et al., 2015). The fine-grained haematite may have been formed by the oxidation of magnetite or the transformation of iron hydroxides. Scanning electron microscope (SEM) imaging indicates the presence of numerous small iron oxides (<2 to 5  $\mu\text{m}$ ) but our observations are not sufficient to confirm a detrital or authigenic origin of these iron oxides.

Yet, regardless of the exact magnetite origin, we suggest that its abrupt appearance following the underlying inconsistent magnetostratigraphy might indicate the presence of an unconformity at the base of the middle Qijiachuan Formation. A more distinct angular unconformity is observed further below between the Minhe and Qijiachuan Formations (Figure 3e). This unconformity can be recognized throughout the basin (He et al., 2021; QBGM; 1985), although in some places less obvious as a disconformity with parallel bedding such as in the Sanhe, Dazhai and Ledu sections (Figure 2). Age constraints on the lower Qijiachuan Formation occurring between these

unconformities are limited, but ostracods and palynomorphs suggest a Cretaceous-to-Palaeocene age (Horton et al., 2004). We also note that the accumulation rates in the early Honggou Formation are extremely low (ca. 0.5 cm/ka in C23n and C22r; Figure 9), which may indicate additional minor unconformities, even though we do not observe any lithological evidence for this.

In conclusion, the early Palaeogene strata of the Xining Basin are marked by at least one, but possibly several unconformities and variable sedimentation rates, both in time and laterally between sections. This infill pattern is in stark contrast to the stable accumulation rates of 2–3 cm/ka observed in the overlying Palaeogene and Neogene strata (Dai et al., 2006; Meijer et al., 2019; Weilin et al., 2017; Xiao et al., 2012; Yang, Yang, et al., 2019). In the following, we will discuss this infill pattern in view of the regional tectonic setting.

## 5.2 | Tectonic implications

The north-eastern Tibetan Plateau is located between two tectonic regimes that dominate the region (e.g. Ratschbacher et al., 2003; Zhang et al., 2019; Zhuang et al., 2018). On the one hand is the subduction of the Pacific Plate resulting in NW-SE extension and forming

multiple extensional basins in eastern China (e.g. Gilder et al., 1991; Ren et al., 2002). This extensional domain may have extended further inland resulting in the formation of grabens around the Ordos block and north-eastern Tibet (Figure 10; Fan et al., 2019; Mercier et al., 2013; Ratschbacher et al., 2003; Wang et al., 2013; Zhang et al., 2003). On the other hand, the India-Asia collision resulted in SW to NE shortening and, mostly left-lateral, strike-slip faulting (Figure 10; e.g. Ratschbacher et al., 2003; Tapponnier et al., 2001; Yuan et al., 2013; Zuza & Yin, 2016). The far-field effects of the collision may have propagated quickly to the north-eastern margin of the Tibetan Plateau (e.g. Clark et al., 2010; Jolivet et al., 2001; Liu, Zhang, Lease, et al., 2013; Yin et al., 2008; Yuan et al., 2013), soon after the collision starting at ca. 60 Ma (e.g. Hu et al., 2016; Kapp & DeCelles, 2019). This has been supported by numerous thermochronological studies indicating early Eocene exhumation in various mountain ranges including the Altyn Tagh, Qilian Shan, East Kunlun Shan and Western Qinling Shan (Figure 10; Clark et al., 2010; He et al., 2017, 2018, 2020; Jolivet et al., 2001; Li et al., 2020; Staisch et al., 2020). The formation of several flexural basins has been linked to this tectonic loading such as the Chaka Basin at 11 Ma (Zhang et al., 2012), the Gonghe Basin at 20 Ma (Craddock et al., 2011) and the Qaidam Basin (Figure 10; Wang et al., 2021) starting either at 51 Ma ('old ages' model; e.g. Ji et al., 2017; Yin et al., 2008) or at 25.5 Ma ('young ages' model; Nie et al., 2020; Wang et al., 2017).

It remains debated whether the Palaeogene Xining Basin formed due to flexure like the Qaidam Basin located in the west or an extensional setting similar to the grabens in the east. Other sub-basins of the Longzhong Basin such as the neighbouring Xunhua-Guide and Linxia Basins show a thickening of the Neogene strata towards the Western Qinling Shan in the south, which supports a developing foredeep due to tectonic loading (Figures 10 and 11a; Fang et al., 2003, 2016; Liu, Zhang, Pan, et al., 2013). Increased exhumation of the Western Qinling Shan started already at ca. 50–45 Ma (Clark et al., 2010; Duvall et al., 2011), which closely corresponds to the onset of deposition in the Linxia Basin at ca. 54–53 Ma (C24n; Feng et al., 2022) and possibly the Xining Basin at >53 Ma. However, we note that the infill pattern of the Xining Basin is not characteristic of a typical foreland basin. Accumulation rates are relatively low throughout for the Palaeogene (ca. 3 cm/kyr, except for the early Eocene), and no coarsening upward trend typical for foredeep propagation (e.g. DeCelles & Giles, 1996) is observed. Increasing accumulation rates and coarsening lithologies only occur ca. 40 million years later during the Neogene uplift of various mountain ranges segmenting the Longzhong Basin

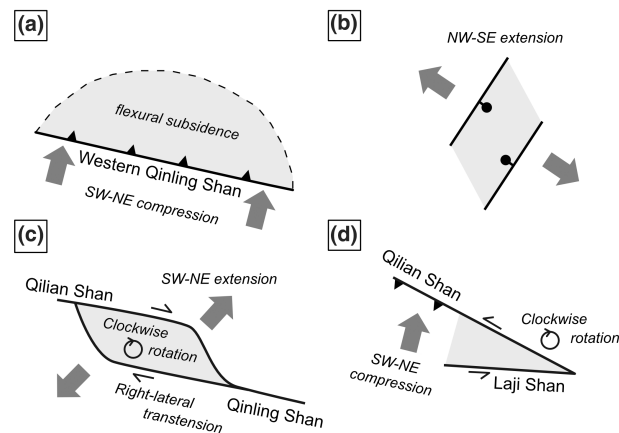


**FIGURE 11** Tectonic models for the origin of the Xining Basin: (a) Foreland basin of the Western Qinling Shan (Fang et al., 2003, 2016; He et al., 2021; Liu, Zhang, Pan, et al., 2013). (b) Extensional basin due to normal faulting (Fan et al., 2019). (c) Right-lateral transtensional basin due to SW–NE extension (Wang et al., 2013, 2016). (d) Left-lateral transtensional basin due to differential rotation of crustal blocks (Zhang et al., 2016).

(Fang et al., 2016; He et al., 2021; Hough et al., 2014; Lease et al., 2011, 2012; Xiao et al., 2012; Yang et al., 2017).

In contrast, extensional basins are characterized by numerous smaller depocenters during the initiation phase, before coalescing into a larger and more stable basin during the later stages (Gawthorpe & Leeder, 2000). This model better explains the local and variable accumulation rates observed in the Xining Basin between 52.9 and 49.7 Ma, followed by low but stable accumulation of the overlying strata. Our study, therefore, supports an extensional origin for the Palaeogene Xining Basin, which could be linked to the development of nearby Eocene grabens such as the Weihe Basin and other half-grabens in the eastern part of the Qinling Shan (Figure 10; Chen et al., 2021; Liu, Zhang, Lease, et al., 2013; Ratschbacher et al., 2003). However, the exact dynamics driving this extension remain unclear. Fan et al. (2019) report various normal faults in the Xining strata, indicating a NW–SE extensional regime (Figure 11b; Fan et al., 2019). Key features are the east and west Shenjiaxia faults and normal faults in the overlying mudrocks, both located ca. 2 km south of the Ledu section (Fan et al., 2019). However, here we note that these faults and mudrocks are not part of the Palaeogene Xining Group as suggested by Fan et al. (2019), but are likely of Cretaceous age because they occur only in the strata below the sandstones of the Minhe Formation. These observations are consistent with an older Cretaceous phase of extension in the Xining Basin (Horton et al., 2004), which is well-documented throughout the region and linked to back-arc spreading and/or intracontinental rifting (e.g. Gilder et al., 1991; Ren et al., 2002).



Wang et al. (2013, 2016) have proposed a renewed phase of SW-to-NE extension during the Eocene. This would have resulted in right lateral movement of the basin-bounding faults, thereby forming the Longzhong Basin (Figure 11c), before the faults were inverted to the left-lateral sense of movement observed today (Figure 10). This is based on structural and stratigraphic observations from the north-eastern margin of the Longzhong Basin and supported by the clockwise rotation observed in the palaeomagnetic data of the Xining Basin between 40 and 29 Ma (Dupont-Nivet et al., 2004; Dupont-Nivet, Dai, et al., 2008). Both Fan et al. (2019) and Wang et al. (2013) suggest that this Eocene extension is driven by the slow-down of convergence and possibly slab rollback of the Pacific Plate (Northrup et al., 1995; Zhuang et al., 2018). Alternatively, the far-field effects of the India–Asia collision could have driven the differential rotation of crustal blocks, thereby forming the Xining Basin through transtension (Figure 11d; Zhang et al., 2016). The continued growth of the northern Tibetan Plateau would have played an increasingly important role throughout the late Palaeogene and Neogene and may have driven additional flexural or transtensional subsidence thereby enlarging the Longzhong Basin (Fang et al., 2003, 2016; Lease et al., 2012; Liu, Zhang, Pan, et al., 2013; Wang et al., 2016).

## 6 | CONCLUSION

The early Eocene sections of the Xining Basin reveal a complex stratigraphy with lateral variability and unconformities. However, by using litho- and magnetostratigraphic correlations throughout the basin, we were able to extend the age model down to the early Eocene at 53.0 Ma (C24n.1r). The stratigraphy reveals an unstable pattern of basin infill between 52.9 and 49.7 Ma (C23n to C22r) with variable accumulation rates ranging from 0.5 to 8 cm/ka. This is in stark contrast to the stable accumulation rates of 2 to 3 cm/ka observed in the overlying strata.

This pattern of slow basin infill is not characteristic of a foreland basin as previously suggested (e.g. He et al., 2021; Liu, Zhang, Pan, et al., 2013) but supports an extensional origin of the Xining Basin. Currently, multiple extensional models exist including NW-SE normal faulting (Fan et al., 2019) and right-lateral transtension (Wang et al., 2013, 2016), both related to the subduction of the Pacific Plate, as well as transtension due to far-field effects of the India–Asia collision and the differential rotation of crustal blocks (Zhang et al., 2016). The Xining Basin is located between these tectonic domains and more detailed structural analyses are required to identify the associated faults, date their motion and test the driving mechanisms for an extension.

Nevertheless, our results elucidate the early tectonic evolution of the Cenozoic Xining Basin and highlight the need for basin-scale analyses to deal with the complex stratigraphy of intracontinental basins (e.g. Fang et al., 2016). Furthermore, we provide a detailed lithostratigraphy and age model for future tectonic, sedimentological, palynological and palaeo-environmental studies in the basin.

## ACKNOWLEDGEMENTS

This study was funded by the ERC consolidator grant MAGIC 649081 to GDN and through the VeWA consortium by the LOEWE programme of the Hessen Ministry of Higher Education, Research and the Arts, Germany. We thank Meimei Xiao, Yang Zhang and Femke Saulus for their support in the field and the lab. We also thank Richard Heermance and two anonymous reviewers for their helpful comments. Open Access funding enabled and organized by Projekt DEAL.

## PEER REVIEW

The peer review history for this article is available at <https://publons.com/publon/10.1111/bre.12720>.

## DATA AVAILABILITY STATEMENT

Raw palaeomagnetic data are available at [earthref.org/MagIC/19501](http://earthref.org/MagIC/19501). ChRM directions, VGP's and U–Pb data are available in the [Supporting Information](#).

## ORCID

Niels Meijer  <https://orcid.org/0000-0002-2186-5682>

## REFERENCES

- Abels, H. A., Dupont-Nivet, G., Xiao, G., Bosboom, R., & Krijgsman, W. (2011). Step-wise change of Asian interior climate preceding the Eocene–Oligocene Transition (EOT). *Palaeogeography, Palaeoclimatology, Palaeoecology*, 299(3), 399–412. <https://doi.org/10.1016/j.palaeo.2010.11.028>
- Ahmed, I. A., & Maher, B. A. (2018). Identification and paleoclimatic significance of magnetite nanoparticles in soils. *Proceedings of the National Academy of Sciences of the United States of America*, 115(8), 1736–1741. <https://doi.org/10.1073/pnas.1719186115>
- Bosboom, R. E., Abels, H. A., Hoorn, C., van den Berg, B. C., Guo, Z., & Dupont-Nivet, G. (2014). Aridification in continental Asia after the middle Eocene climatic optimum (MECO). *Earth and Planetary Science Letters*, 389, 34–42. <https://doi.org/10.1016/j.epsl.2013.12.014>
- Bureau of Geological and Mineral Resources of Qinghai Province (BGMRPQ). (1965). *Regional geological survey reports of Ledu sheet (1:200000), Qinghai Province, P.R. China (in Chinese)*.
- Chen, X., Dong, S., Shi, W., Zuza, A. V., Li, Z., Chen, P., Liu, J., Hu, J., & Han, B. (2021). Magnetostratigraphic ages of the Cenozoic Weihe and Shanxi grabens in North China and their tectonic implications. *Tectonophysics*, 813, 228914. <https://doi.org/10.1016/j.tecto.2021.228914>



- Cheng, F., Jolivet, M., Guo, Z., Wang, L., Zhang, C., & Li, X. (2021). Cenozoic evolution of the Qaidam basin and implications for the growth of the northern Tibetan plateau: A review. *Earth-Science Reviews*, 220, 103730. <https://doi.org/10.1016/j.earscirev.2021.103730>
- Clark, M. K., Farley, K. A., Zheng, D., Wang, Z., & Duvall, A. R. (2010). Early Cenozoic faulting of the northern Tibetan plateau margin from apatite (U–Th)/He ages. *Earth and Planetary Science Letters*, 296(1), 78–88. <https://doi.org/10.1016/j.epsl.2010.04.051>
- Cong, F., Tian, J., Hao, F., Licht, A., Liu, Y., Cao, Z., & Eiler, J. M. (2021). A thermal pulse induced by a Permian mantle plume in the Tarim Basin, Northwest China: Constraints from clumped isotope thermometry and In situ calcite U–Pb dating. *Journal of Geophysical Research: Solid Earth*, 126(4), e2020JB020636. <https://doi.org/10.1029/2020JB020636>
- Craddock, W., Kirby, E., & Zhang, H. (2011). Late Miocene–Pliocene range growth in the interior of the northeastern Tibetan Plateau. *Lithosphere*, 3(6), 420–438. <https://doi.org/10.1130/L159.1>
- Dai, S., Fang, X., Dupont-Nivet, G., Song, C., Gao, J., Krijgsman, W., Langereis, C., & Zhang, W. (2006). Magnetostratigraphy of Cenozoic sediments from the Xining Basin: Tectonic implications for the northeastern Tibetan plateau. *Journal of Geophysical Research: Solid Earth*, 111(B11). <https://doi.org/10.1029/2005JB004187>
- DeCelles, P. G., & Giles, K. A. (1996). Foreland basin systems. *Basin Research*, 8(2), 105–123. <https://doi.org/10.1046/j.1365-2117.1996.01491.x>
- Deng, C., Zhu, R., Verosub, K. L., Singer, M. J., & Vidic, N. J. (2004). Mineral magnetic properties of loess/paleosol couplets of the central loess plateau of China over the last 1.2 Myr. *Journal of Geophysical Research: Solid Earth*, 109(B1). <https://doi.org/10.1029/2003JB002532>
- Dupont-Nivet, G., Horton, B. K., Butler, R. F., Wang, J., Zhou, J., & Waanders, G. L. (2004). Paleogene clockwise tectonic rotation of the Xining-Lanzhou region, northeastern Tibetan plateau. *Journal of Geophysical Research: Solid Earth*, 109(B4). <https://doi.org/10.1029/2003JB002620>
- Dupont-Nivet, G., Krijgsman, W., Langereis, C. G., Abels, H. A., Dai, S., & Fang, X. (2007). Tibetan plateau aridification linked to global cooling at the Eocene–Oligocene transition. *Nature*, 445(7128), 635–638.
- Dupont-Nivet, G., Hoorn, C., & Konert, M. (2008). Tibetan uplift prior to the Eocene–Oligocene climate transition: Evidence from pollen analysis of the Xining Basin. *Geology*, 36(12), 987–990. <https://doi.org/10.1130/G25063A.1>
- Dupont-Nivet, G., Dai, S., Fang, X., Krijgsman, W., Erens, V., Reitsma, M., & Langereis, C. (2008). Timing and distribution of tectonic rotations in the northeastern Tibetan plateau. *Investigations into the Tectonics of the Tibetan Plateau*, 444, 73–87.
- Duvall, A. R., Clark, M. K., van der Pluijm, B. A., & Li, C. (2011). Direct dating of Eocene reverse faulting in northeastern Tibet using Ar-dating of fault clays and low-temperature thermochronometry. *Earth and Planetary Science Letters*, 304(3–4), 520–526. <https://doi.org/10.1016/j.epsl.2011.02.028>
- Fan, L. G., Meng, Q. R., Wu, G. L., Wei, H. H., Du, Z. M., & Wang, E. (2019). Paleogene crustal extension in the eastern segment of the NE Tibetan plateau. *Earth and Planetary Science Letters*, 514, 62–74. <https://doi.org/10.1016/j.epsl.2019.02.036>
- Fang, X., Garzzone, C., Van der Voo, R., Li, J., & Fan, M. (2003). Flexural subsidence by 29 Ma on the NE edge of Tibet from the magnetostratigraphy of Linxia Basin, China. *Earth and Planetary Science Letters*, 210(3–4), 545–560. [https://doi.org/10.1016/S0012-821X\(03\)00142-0](https://doi.org/10.1016/S0012-821X(03)00142-0)
- Fang, X., Zan, J., Appel, E., Lu, Y., Song, C., Dai, S., & Tuo, S. (2015). An Eocene–Miocene continuous rock magnetic record from the sediments in the Xining Basin, NW China: Indication for Cenozoic persistent drying driven by global cooling and Tibetan Plateau uplift. *Geophysical Journal International*, 201(1), 78–89. <https://doi.org/10.1093/gji/ggv002>
- Fang, X., Wang, J., Zhang, W., Zan, J., Song, C., Yan, M., Appel, E., Zhang, T., Wu, F., Yang, Y., & Lu, Y. (2016). Tectonosedimentary evolution model of an intracontinental flexural (foreland) basin for paleoclimatic research. *Global and Planetary Change*, 145, 78–97. <https://doi.org/10.1016/j.gloplacha.2016.08.015>
- Fang, X., Fang, Y., Zan, J., Zhang, W., Song, C., Appel, E., Meng, Q., Miao, Y., Dai, S., Lu, Y., & Zhang, T. (2019). Cenozoic magnetostratigraphy of the Xining Basin, NE Tibetan plateau, and its constraints on paleontological, sedimentological and tectonomorphological evolution. *Earth-Science Reviews*, 190, 460–485. <https://doi.org/10.1016/j.earscirev.2019.01.021>
- Fang, X., Galy, A., Yang, Y., Zhang, W., Ye, C., & Song, C. (2019). Paleogene global cooling-induced temperature feedback on chemical weathering, as recorded in the northern Tibetan plateau. *Geology*, 47(10), 992–996.
- Feng, Z., Zhang, W., Zhang, T., Fang, X., Zan, J., Yan, M., Song, C., Li, T., Ning, W., & Wang, H. (2021). Early-middle Eocene hydroclimate variations recorded by environmental magnetism in the Linxia Basin, NE Tibetan plateau. *Paleoceanography and Paleoclimatology*, 36(11), e2021PA004338. <https://doi.org/10.1029/2021PA004338>
- Feng, Z., Zhang, W., Fang, X., Zan, J., Zhang, T., Song, C., & Yan, M. (2022). Eocene deformation of the NE Tibetan plateau: Indications from magnetostratigraphic constraints on the oldest sedimentary sequence in the Linxia Basin. *Gondwana Research*, 101, 77–93. <https://doi.org/10.1016/j.gr.2021.07.027>
- Fisher, R. (1953). Dispersion on a sphere. *Proceedings of the Royal Society of London A: Mathematical, Physical and Engineering Sciences*, 217(1130), 295–305. <https://doi.org/10.1098/rspa.1953.0064>
- Gawthorpe, R. L., & Leeder, M. R. (2000). Tectono-sedimentary evolution of active extensional basins. *Basin Research*, 12(3–4), 195–218. <https://doi.org/10.1111/j.1365-2117.2000.00121.x>
- Gilder, S. A., Keller, G. R., Luo, M., & Goodell, P. C. (1991). Eastern Asia and the western Pacific timing and spatial distribution of rifting in China. *Tectonophysics*, 197(2–4), 225–243. [https://doi.org/10.1016/0040-1951\(91\)90043-RGet](https://doi.org/10.1016/0040-1951(91)90043-RGet)
- He, C. C., Zhang, Y. Q., Li, S. K., Wang, K., & Ji, J. Q. (2021). Magnetostratigraphic study of a late cretaceous–Paleogene succession in the eastern Xining basin, NE Tibet: Constraint on the timing of major tectonic events in response to the India–Eurasia collision. *GSA Bulletin*, 133, 2457–2484. <https://doi.org/10.1130/B35874.1>
- He, P., Song, C., Wang, Y., Chen, L., Chang, P., Wang, Q., & Ren, B. (2017). Cenozoic exhumation in the Qilian Shan, northeastern Tibetan plateau: Evidence from detrital fission track thermochronology in the Jiuquan Basin. *Journal of Geophysical Research - Solid Earth*, 122, 6910–6927. <https://doi.org/10.1002/2017JB014216>

- He, P., Song, C., Wang, Y., Meng, Q., Chen, L., Yao, L., Huang, R., Feng, W., & Chen, S. (2018). Cenozoic deformation history of the Qilian Shan (northeastern Tibetan plateau) constrained by detrital apatite fission-track thermochronology in the northeastern Qaidam Basin. *Tectonophysics*, 749, 1–11. <https://doi.org/10.1016/j.tecto.2018.10.017>
- He, P., Song, C., Wang, Y., Meng, Q., Wang, D., Feng, Y., Chen, L., & Feng, W. (2020). Early Cenozoic exhumation in the Qilian Shan, northeastern margin of the Tibetan plateau: Insights from detrital apatite fission track thermochronology. *Terra Nova*, 32(6), 415–424. <https://doi.org/10.1111/ter.12478>
- Hoorn, C., Straathof, J., Abels, H. A., Xu, Y., Utescher, T., & Dupont-Nivet, G. (2012). A late Eocene palynological record of climate change and Tibetan plateau uplift (Xining Basin, China). *Palaeogeography, Palaeoclimatology, Palaeoecology*, 344, 16–38. <https://doi.org/10.1016/j.palaeo.2012.05.011>
- Horton, B. K., Dupont-Nivet, G., Zhou, J., Waanders, G. L., Butler, R. F., & Wang, J. (2004). Mesozoic-Cenozoic evolution of the Xining-Minhe and Dangchang basins, northeastern Tibetan plateau: Magnetostratigraphic and biostratigraphic results. *Journal of Geophysical Research: Solid Earth*, 109(B4). <https://doi.org/10.1029/2003JB002913>
- Hough, B. G., Garzzone, C. N., Wang, Z., Lease, R. O., Nie, J., Horton, B. K., & Hoke, G. D. (2014). Timing and spatial patterns of basin segmentation and climate change in northeastern Tibet. Toward an improved understanding of uplift mechanisms and the elevation history of the Tibetan Plateau. *Geological Society of America Special Paper*, 507, 129–153.
- Hu, X., Garzanti, E., Wang, J., Huang, W., An, W., & Webb, A. (2016). The timing of India-Asia collision onset—facts, theories, controversies. *Earth-Science Reviews*, 160, 264–299. <https://doi.org/10.1016/j.earscirev.2016.07.014>
- Ji, J., Zhang, K., Clift, P. D., Zhuang, G., Song, B., Ke, X., & Xu, Y. (2017). High-resolution magnetostratigraphic study of the Paleogene-Neogene strata in the northern Qaidam Basin: Implications for the growth of the northeastern Tibetan plateau. *Gondwana Research*, 46, 141–155. <https://doi.org/10.1016/j.gr.2017.02.015>
- Jolivet, M., Brunel, M., Seward, D., Xu, Z., Yang, J., Roger, F., Tapponnier, P., Malavieille, J., Arnaud, N., & Wu, C. (2001). Mesozoic and Cenozoic tectonics of the northern edge of the Tibetan plateau: Fission-track constraints. *Tectonophysics*, 343(1–2), 111–134. [https://doi.org/10.1016/S0040-1951\(01\)00196-2](https://doi.org/10.1016/S0040-1951(01)00196-2)
- Kapp, P., & DeCelles, P. G. (2019). Mesozoic–Cenozoic geological evolution of the Himalayan-Tibetan orogen and working tectonic hypotheses. *American Journal of Science*, 319(3), 159–254. <https://doi.org/10.2475/03.2019.01>
- Kirschvink, J. L. (1980). The least-squares line and plane and the analysis of palaeomagnetic data. *Geophysical Journal International*, 62(3), 699–718. <https://doi.org/10.1111/j.1365-246X.1980.tb02601.x>
- Lease, R. O., Burbank, D. W., Clark, M. K., Farley, K. A., Zheng, D., & Zhang, H. (2011). Middle Miocene reorganization of deformation along the northeastern Tibetan plateau. *Geology*, 39(4), 359–362. <https://doi.org/10.1130/G31356.1>
- Lease, R. O., Burbank, D. W., Hough, B., Wang, Z., & Yuan, D. (2012). Pulsed Miocene range growth in northeastern Tibet: Insights from Xunhua Basin magnetostratigraphy and provenance. *Bulletin*, 124(5–6), 657–677. <https://doi.org/10.1130/B30524.1>
- Li, J. X., Yue, L. P., Roberts, A. P., Hirt, A. M., Pan, F., Guo, L., Xu, Y., Xi, R. G., Guo, L., Qiang, X. K., Gai, C. C., Jiang, Z. X., Sun, Z. M., & Liu, Q. S. (2018). Global cooling and enhanced Eocene Asian mid-latitude interior aridity. *Nature Communications*, 9(1), 3026. <https://doi.org/10.1038/s41467-018-05415-x>
- Li, B., Zuza, A. V., Chen, X., Hu, D., Shao, Z., Qi, B., Wang, Z., Levy, D. A., & Xiong, X. (2020). Cenozoic multi-phase deformation in the Qilian Shan and out-of-sequence development of the northern Tibetan plateau. *Tectonophysics*, 782, 228423. <https://doi.org/10.1016/j.tecto.2020.228423>
- Licht, A., Van Cappelle, M., Abels, H. A., Ladant, J. B., Trabuccho-Alexandre, J., France-Lanord, C., Donnadieu, Y., Vandenberghe, J., Rigaudier, T., Lécuyer, C., Terry, D., Jr., Adriaens, R., Boura, A., Guo, Z., Soe, A. N., Quade, J., Dupont-Nivet, G., & Jaeger, J.-J. (2014). Asian monsoons in a late Eocene greenhouse world. *Nature*, 513(7519), 501–506. <https://doi.org/10.1038/nature13704>
- Licht, A., Dupont-Nivet, G., Pullen, A., Kapp, P., Abels, H. A., Lai, Z., Guo, Z., Abell, J., & Giesler, D. (2016). Resilience of the Asian atmospheric circulation shown by Paleogene dust provenance. *Nature Communications*, 7, 12390. <https://doi.org/10.1038/ncomms12390>
- Licht, A., Dupont-Nivet, G., Meijer, N., Rugenstein, J. C., Schauer, A., Fiebig, J., Mulch, A., Hoorn, C., & Guo, Z. (2020). Decline of soil respiration in northeastern Tibet through the transition into the Oligocene icehouse. *Palaeogeography, Palaeoclimatology, Palaeoecology*, 560, 110016. <https://doi.org/10.1016/j.palaeo.2020.110016>
- Licht, A., Win, Z., Westerweel, J., Cogné, N., Morley, C. K., Chantraprasert, S., Poblete, F., Ugrai, T., Nelson, B., Aung, D. W., & Dupont-Nivet, G. (2020). Magmatic history of Central Myanmar and implications for the evolution of the Burma terrane. *Gondwana Research*, 87, 303–319. <https://doi.org/10.1016/j.gr.2020.06.016>
- Liu, J., Zhang, P., Lease, R. O., Zheng, D., Wan, J., Wang, W., & Zhang, H. (2013). Eocene onset and late Miocene acceleration of Cenozoic intracontinental extension in the North Qinling range–Weihe graben: Insights from apatite fission track thermochronology. *Tectonophysics*, 584, 281–296. <https://doi.org/10.1016/j.tecto.2012.01.025>
- Liu, S., Zhang, G., Pan, F., Zhang, H., Wang, P., Wang, K., & Wang, Y. (2013). Timing of Xunhua and guide basin development and growth of the northeastern Tibetan plateau, China. *Basin Research*, 25(1), 74–96. <https://doi.org/10.1111/j.1365-2117.2012.00548.x>
- Maher, B. A., & Taylor, R. M. (1988). Formation of ultrafine-grained magnetite in soils. *Nature*, 336(6197), 368–370. <https://doi.org/10.1038/336368a0>
- McFadden, P. L., & McElhinny, M. W. (1990). Classification of the reversal test in palaeomagnetism. *Geophysical Journal International*, 103(3), 725–729. <https://doi.org/10.1111/j.1365-246X.1990.tb05683.x>
- Meijer, N., Dupont-Nivet, G., Abels, H. A., Kaya, M. Y., Licht, A., Xiao, M., Zhang, Y., Roperch, P., Poujol, M., Lai, Z., & Guo, Z. (2019). Central Asian moisture modulated by proto-Paratethys Sea incursions since the early Eocene. *Earth and Planetary Science Letters*, 510, 73–84. <https://doi.org/10.1016/j.epsl.2018.12.031>

- Meijer, N., Dupont-Nivet, G., Barbolini, N., Woutersen, A., Rohrmann, A., Zhang, Y., Liu, X. J., Licht, A., Abels, H. A., Hoorn, C., Tjallingii, R., Andermann, C., Dietze, M., & Nowaczyk, N. (2021). Loess-like dust appearance at 40 Ma in Central China. *Paleoceanography and Paleoclimatology*, *36*(3), e2020PA003993. <https://doi.org/10.1029/2020PA003993>
- Mercier, J. L., Vergely, P., Zhang, Y. Q., Hou, M. J., Bellier, O., & Wang, Y. M. (2013). Structural records of the late Cretaceous–Cenozoic extension in Eastern China and the kinematics of the Southern Tan-Lu and Qinling fault zone (Anhui and Shaanxi provinces, PR China). *Tectonophysics*, *582*, 50–75. <https://doi.org/10.1016/j.tecto.2012.09.015>
- Nie, J., Ren, X., Saylor, J. E., Su, Q., Horton, B. K., Bush, M. A., Chen, W., & Pfaff, K. (2020). Magnetic polarity stratigraphy, provenance, and paleoclimate analysis of Cenozoic strata in the Qaidam Basin, NE Tibetan Plateau. *GSA Bulletin*, *132*(1–2), 310–320. <https://doi.org/10.1130/B35175.1>
- North, C. P., & Davidson, S. K. (2012). Unconfined alluvial flow processes: Recognition and interpretation of their deposits, and the significance for palaeogeographic reconstruction. *Earth-Science Reviews*, *111*(1), 199–223. <https://doi.org/10.1016/j.earscirev.2011.11.008>
- Northrup, C. J., Royden, L. H., & Burchfiel, B. C. (1995). Motion of the Pacific plate relative to Eurasia and its potential relation to Cenozoic extension along the eastern margin of Eurasia. *Geology*, *23*(8), 719–722. [https://doi.org/10.1130/0091-7613\(1995\)023<0719:MOTPPR>2.3.CO;2](https://doi.org/10.1130/0091-7613(1995)023<0719:MOTPPR>2.3.CO;2)
- Page, M., Licht, A., Dupont-Nivet, G., Meijer, N., Barbolini, N., Hoorn, C., Schauer, A., Huntington, K., Bajnai, D., Fiebig, J., & Mulch, A. (2019). Synchronous cooling and decline in monsoonal rainfall in northeastern Tibet during the fall into the Oligocene icehouse. *Geology*, *47*(3), 203–206. <https://doi.org/10.1130/G45480.1>
- Qinghai Bureau of Geology and Mineral Resources (QBGMR). (1985). *Geologic maps of the Duoba, Gaodian, Tianjiazai, and Xining regions (4 sheets), with regional geologic report (1:50,000 scale)* (p. 199).
- Ratschbacher, L., Hacker, B. R., Calvert, A., Webb, L. E., Grimmer, J. C., McWilliams, M. O., Ireland, T., Dong, S., & Hu, J. (2003). Tectonics of the Qinling (Central China): Tectonostratigraphy, geochronology, and deformation history. *Tectonophysics*, *366* (1–2), 1–53. [https://doi.org/10.1016/S0040-1951\(03\)00053-2](https://doi.org/10.1016/S0040-1951(03)00053-2)
- Ren, J., Tamaki, K., Li, S., & Junxia, Z. (2002). Late Mesozoic and Cenozoic rifting and its dynamic setting in eastern China and adjacent areas. *Tectonophysics*, *344*(3–4), 175–205. [https://doi.org/10.1016/S0040-1951\(01\)00271-2](https://doi.org/10.1016/S0040-1951(01)00271-2)
- Roberts, A. P., Cui, Y., & Verosub, K. L. (1995). Wasp-waisted hysteresis loops: Mineral magnetic characteristics and discrimination of components in mixed magnetic systems. *Journal of Geophysical Research: Solid Earth*, *100*(B9), 17909–17924. <https://doi.org/10.1029/95JB00672>
- Ruan, X., Yang, Y., Galy, A., Fang, X., Jin, Z., Zhang, F., Yang, R., Deng, L., Meng, Q., Ye, C., & Zhang, W. (2019). Evidence for early ( $\geq 12.7$  Ma) eolian dust impact on river chemistry in the northeastern Tibetan plateau. *Earth and Planetary Science Letters*, *515*, 79–89. <https://doi.org/10.1016/j.epsl.2019.03.022>
- Ryan, W. B. F., Carbotte, S. M., Coplan, J., O'Hara, S., Melkonian, A., Arko, R., Weissel, R. A., Ferrini, V., Goodwillie, A., Nitsche, F., Bonczkowski, J., & Zemsky, R. (2009). Global multi-resolution topography (GMRT) synthesis data set. *Geochemistry, Geophysics, Geosystems*, *10*, Q03014. <https://doi.org/10.1029/2008GC002332>
- Smoot, J. P., & Lowenstein, T. K. (1991). Depositional environments of non-marine evaporites. *Developments in Sedimentology*, *50*, 189–347. [https://doi.org/10.1016/S0070-4571\(08\)70261-9](https://doi.org/10.1016/S0070-4571(08)70261-9)
- Speijer, R. P., Pälke, H., Hollis, C. J., Hooker, J. J., & Ogg, J. G. (2020). The paleogene period. In F. M. Gradstein, J. G. Ogg, M. D. Schmitz, G. M. Ogg, *Geologic Time Scale 2020* (Eds.), *Geologic time scale 2020* (pp. 1087–1140). Elsevier.
- Staisch, L. M., Niemi, N. A., Clark, M. K., & Chang, H. (2020). The Cenozoic evolution of crustal shortening and left-lateral shear in the central east Kunlun Shan: Implications for the uplift history of the Tibetan plateau. *Tectonics*, *39*, e2020TC006065. <https://doi.org/10.1029/2020TC006065>
- Talbot, M. R., Holm, K., & Williams, M. A. J. (1994). Sedimentation in low-gradient desert margin systems: A comparison of the late Triassic of Northwest Somerset (England) and the late quaternary of east-Central Australia. *Geological Society of America Special Papers*, *289*, 97–117.
- Tapponnier, P., Zhiqin, X., Roger, F., Meyer, B., Arnaud, N., Wittlinger, G., & Jingsui, Y. (2001). Oblique stepwise rise and growth of the Tibet plateau. *Science*, *294*(5547), 1671–1677. <https://doi.org/10.1126/science.105978>
- Wang, W., Kirby, E., Peizhen, Z., Dewen, Z., Guangliang, Z., Huiping, Z., Wenjun, Z., & Chizhang, C. (2013). Tertiary basin evolution along the northeastern margin of the Tibetan plateau: Evidence for basin formation during Oligocene transtension. *Bulletin*, *125*(3–4), 377–400. <https://doi.org/10.1130/B30611.1>
- Wang, W., Zhang, P., Liu, C., Zheng, D., Yu, J., Zheng, W., Wang, Y., Zhang, H., & Chen, X. (2016). Pulsed growth of the west Qinling at ~30 Ma in northeastern Tibet: Evidence from Lanzhou Basin magnetostratigraphy and provenance. *Journal of Geophysical Research: Solid Earth*, *121*(11), 7754–7774. <https://doi.org/10.1002/2016JB013279>
- Wang, L., Cheng, F., Zuza, A. V., Jolivet, M., Liu, Y., Guo, Z., Li, X., & Zhang, C. (2021). Diachronous growth of the northern Tibetan plateau derived from flexural modeling. *Geophysical Research Letters*, *48*(8), e2020GL092346. <https://doi.org/10.1029/2020GL092346>
- Wang, W., Zheng, W., Zhang, P., Li, Q., Kirby, E., Yuan, D., Zheng, D., Liu, C., Zhang, H., & Pang, J. (2017). Expansion of the Tibetan Plateau during the Neogene. *Nature Communications*, *8*(1), 1–12. <https://doi.org/10.1038/ncomms15887>
- Weilin, Z., Tao, Z., Chunhui, S., Appel, E., Ziqiang, M., Yahui, F., Yin, L., Qingquan, M., Rongsheng, Y., Dawen, Z., Bingshuai, L., & Jiao, L. (2017). Termination of fluvial-alluvial sedimentation in the Xining Basin, NE Tibetan Plateau, and its subsequent geomorphic evolution. *Geomorphology*, *297*, 86–99. <https://doi.org/10.1016/j.geomorph.2017.09.008>
- Westerhold, T., Marwan, N., Drury, A. J., Liebrand, D., Agnini, C., Anagnostou, E., Barnet, J. S. K., Bohaty, S. M., De Vleeschouwer, D., Florindo, F., Frederichs, T., Hodell, D. A., Holbourn, A. E., Kroon, D., Lauretano, V., Littler, K., Lourens, L. J., Lyle, M., Pälke, H., ... Zachos, J. C. (2020). An astronomically dated record of Earth's climate and its predictability over the last 66 million years. *Science*, *369*(6509), 1383–1387. <https://doi.org/10.1126/science.aba6853>
- Xiao, G., Guo, Z., Dupont-Nivet, G., Lu, H., Wu, N., Ge, J., Hao, Q., Peng, S., Li, F., Abels, H. A., & Zhang, K. (2012). Evidence for northeastern Tibetan plateau uplift between 25 and 20 Ma in the



- sedimentary archive of the Xining Basin, northwestern China. *Earth and Planetary Science Letters*, 317, 185–195. <https://doi.org/10.1016/j.epsl.2011.11.008>
- Yang, R., Fang, X., Meng, Q., Zan, J., Zhang, W., Deng, T., Yang, Y., Ruan, X., Yang, L., & Li, B. (2017). Paleomagnetic constraints on the middle Miocene-early Pliocene stratigraphy in the Xining Basin, NE Tibetan plateau, and the geologic implications. *Geochemistry, Geophysics, Geosystems*, 18(11), 3741–3757. <https://doi.org/10.1002/2017GC006945>
- Yang, R., Yang, Y., Fang, X., Ruan, X., Galy, A., Ye, C., Meng, Q., & Han, W. (2019). Late miocene intensified tectonic uplift and climatic aridification on the northeastern Tibetan plateau: Evidence from clay mineralogical and geochemical records in the Xining Basin. *Geochemistry, Geophysics, Geosystems*, 20(2), 829–851.
- Yang, F., Guo, Z., Zhang, C., Abu Sadat Md, S., He, Z., & Deng, C. (2019). High-resolution Eocene magnetostratigraphy of the Xijigou section: Implications for the infilling process of Xining Basin, northeastern Tibetan plateau. *Journal of Geophysical Research: Solid Earth*, 124(8), 7588–7603. <https://doi.org/10.1029/2019JB017624>
- Yin, A., Dang, Y. Q., Wang, L. C., Jiang, W. M., Zhou, S. P., Chen, X. H., Gehrels, G. E., & McRivette, M. W. (2008). Cenozoic tectonic evolution of Qaidam basin and its surrounding regions (part 1): The southern Qilian Shan-Nan Shan thrust belt and northern Qaidam basin. *Geological Society of America Bulletin*, 120(7–8), 813–846. <https://doi.org/10.1130/B26180.1>
- Yuan, D. Y., Ge, W. P., Chen, Z. W., Li, C. Y., Wang, Z. C., Zhang, H. P., Zhang, P. Z., Zheng, D. W., Zheng, W. J., Craddock, W. H., Dayem, K. E., Duvall, A. R., Hough, B. G., Lease, R. O., Champagnac, J. D., Burbank, D. W., Clark, M. K., Farley, K. A., Garzione, C. N., ... Roe, G. H. (2013). The growth of northeastern Tibet and its relevance to large-scale continental geodynamics: A review of recent studies. *Tectonics*, 32(5), 1358–1370. <https://doi.org/10.1002/tect.20081>
- Zhang, Y. Q., Ma, Y., Yang, N., Shi, W., & Dong, S. (2003). Cenozoic extensional stress evolution in North China. *Journal of Geodynamics*, 36(5), 591–613. <https://doi.org/10.1016/j.jog.2003.08.001>
- Zhang, H. P., Craddock, W. H., Lease, R. O., Wang, W. T., Yuan, D. Y., Zhang, P. Z., Molnar, P., Zheng, D. W., & Zheng, W. J. (2012). Magnetostratigraphy of the Neogene Chaka basin and its implications for mountain building processes in the north-eastern Tibetan plateau. *Basin Research*, 24(1), 31–50. <https://doi.org/10.1111/j.1365-2117.2011.00512.x>
- Zhang, J., & Cunningham, D. (2013). Polyphase transpressional development of a NNE-striking basement-cored anticline in the Xining Basin, northeastern Qinghai–Tibetan Plateau. *Geological Magazine*, 150(4), 626–638. <https://doi.org/10.1017/S0016756812000866>
- Zhang, J., Wang, Y., Zhang, B., & Zhang, Y. (2016). Tectonics of the Xining Basin in NW China and its implications for the evolution of the NE Qinghai-Tibetan plateau. *Basin Research*, 28(2), 159–182. <https://doi.org/10.1111/bre.12104>
- Zhang, Y., Dong, S., & Li, J. (2019). Late Paleogene sinistral strike-slip system along east Qinling and in southern North China: Implications for interaction between collision-related block trans-rotation and subduction-related back-arc extension in East China. *Tectonophysics*, 769, 228181. <https://doi.org/10.1016/j.tecto.2019.228181>
- Zhuang, G., Johnstone, S. A., Hourigan, J., Ritts, B., Robinson, A., & Sobel, E. R. (2018). Understanding the geologic evolution of northern Tibetan plateau with multiple thermochronometers. *Gondwana Research*, 58, 195–210. <https://doi.org/10.1016/j.gr.2018.02.014>
- Zuza, A. V., & Yin, A. (2016). Continental deformation accommodated by non-rigid passive bookshelf faulting: An example from the Cenozoic tectonic development of northern Tibet. *Tectonophysics*, 677, 227–240. <https://doi.org/10.1016/j.tecto.2016.04.007>

## SUPPORTING INFORMATION

Additional supporting information can be found online in the Supporting Information section at the end of this article.

**How to cite this article:** Meijer, N., Dupont-Nivet, G., Licht, A., Roperch, P., Rohrmann, A., Sun, A., Lu, S., Woutersen, A., & Nowaczyk, N. (2023). Early Eocene magnetostratigraphy and tectonic evolution of the Xining Basin, NE Tibet. *Basin Research*, 35, 510–529. <https://doi.org/10.1111/bre.12720>